Nanoscale

ROYAL SOCIETY OF CHEMISTRY

REVIEW

View Article Online
View Journal | View Issue

Cite this: *Nanoscale*, 2022, **14**, 8216

Progress in the use of organic potassium salts for the synthesis of porous carbon nanomaterials: microstructure engineering for advanced supercapacitors

Qian Zhang,*†[a] Bing Yan,†[b] Li Feng,†[b] Jiaojiao Zheng,[b] Bo You,*[c] Jiayun Chen,[a] Xin Zhao,*[d] Chunmei Zhang,[e] Shaohua Jiang[b] and Shuijian He*[b]

Porous carbon nanomaterials (PCNs) are widely applied in energy storage devices. Traditionally, PCNs were mainly synthesized by activation and templating methods, which are time-consuming, tedious, corrosive and relatively high cost. Therefore, the development of easier and greener methods to produce PCNs is of great significance. Recently, organic potassium salts (OPSs) emerged as versatile reagents for synthesizing PCNs. The OPS-based synthesis of PCNs can avoid the use of large amounts of corrosive chemical agents. Potassium carbonate generated *in situ* from the decomposition of OPSs could serve as both a green activation agent and a water-removable template to produce nanopores. Potassium oxide and potassium formed at higher temperature could generate additional porosity, contributing to a highly porous architecture. The carbon-rich organic moiety could function as a carbon precursor and chemical blowing agent. This review aims to elucidate the multifunctionality of OPSs in the synthesis of PCNs and the capacitive performance of the corresponding PCNs. To this end, recent progress on the capacitive performance of PCNs synthesized from OPSs is summarized. This review provides constructive viewpoints for the cost-effective and green synthesis of PCNs with the aid of OPSs for application in supercapacitors.

Received 11th April 2022,
Accepted 10th May 2022

DOI: 10.1039/d2nr01986h

rsc.li/nanoscale

1. Introduction

Porous carbon nanomaterials (PCNs) are promising materials for energy storage devices, including supercapacitors (SCs), lithium-ion and lithium-sulfur batteries, CO_2 capture, dye absorption, and other fields.[1–7] According to the classification of the International Union of Pure and Applied Chemistry, nanopores in porous materials are divided into micropores (<2 nm), mesopores (2–50 nm), and macropores (>50 nm).[8–10] For SCs, macropores make a major contribution to the total pore volume (V_t) of PCNs and serve as reservoirs for electrolyte ions while mesopores function as the diffusion channels for electrolyte ions. Compared with mesopores and macropores, micropores play a dominant role in ion storage and they contribute more to the specific surface area (SSA) and specific capacitance (C_{sp}).[11–13] PCNs can be obtained by the pyrolysis of various carbon precursors with templates and/or activation agents.[14–23] PCNs prepared by a template-assisted process usually exhibit a meso-/macro-pore dominated architecture with a relatively low SSA (<500 $m^2\ g^{-1}$) and small C_{sp} (<200 F g^{-1}),[24–26] while PCNs prepared by an activation agent based synthesis usually exhibit micropore-dominated porosity with quite a high SSA (>1000 $m^2\ g^{-1}$) and much larger C_{sp} (>300 F g^{-1}).[16,27,28] Therefore, activation is considered to be an effective approach for enhancing the capacitance performance of PCNs, and various activation agents have been explored.[29–32]

Nowadays, PCNs can be produced on an industrial scale by traditional carbonization–activation procedures. In general, activation can be divided into physical activation and chemical activation (Fig. 1).[11,33–35] Steam, CO_2, and air (in fact O_2 plays the role) are often used as activation agents in physical

[a]College of Science, Nanjing Forestry University, Nanjing 210037, China. E-mail: zhangqian5689@njfu.edu.cn
[b]Co-Innovation Center of Efficient Processing and Utilization of Forest Resources, College of Materials Science and Engineering, Nanjing Forestry University, Nanjing 210037, China. E-mail: shuijianhe@njfu.edu.cn
[c]Key Laboratory of Material Chemistry for Energy Conversion and Storage, Ministry of Education, Hubei Key Laboratory of Material Chemistry and Service Failure, School of Chemistry and Chemical Engineering, Huazhong University of Science and Technology (HUST), Wuhan, Hubei 430074, China. E-mail: youbo@hust.edu.cn
[d]School of Science, Wuhan University of Technology, Wuhan, Hubei 430070, China. E-mail: xzhao@whut.edu.cn
[e]Institute of Materials Science and Devices, School of Materials Science and Engineering, Suzhou University of Science and Technology, Suzhou 215009, China
†These authors contributed equally to this work.

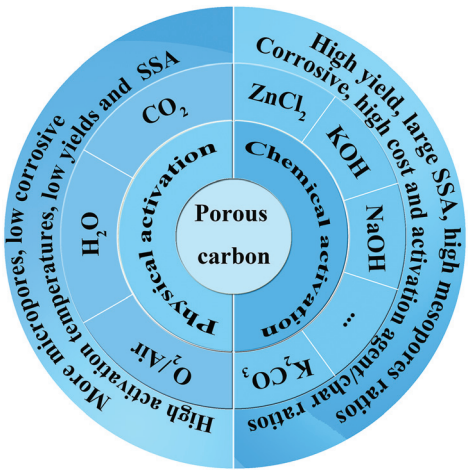

Fig. 1 Comparison of physical activation and chemical activation in the synthesis of porous carbon.

activation.[15,36–45] Pores are generated by the oxidation–reduction reactions between the activation agents and carbon matrix during the physical activation process (eqn (1)–(3)).[46]

$$C + H_2O \rightarrow CO + H_2 \quad (1)$$

$$C + CO_2 \rightarrow CO \quad (2)$$

$$C + O_2 \rightarrow CO_2 \quad (3)$$

Although the agents involved in physical activation are less corrosive,[47–51] physical activation usually requires a longer activation time, a higher activation temperature, and results in relatively lower yields, smaller pore sizes, lower SSAs and a lower tap density compared to chemical activation.[73,54]

Chemical activations, on the other hand, possess the advantages of high yields and mild activation conditions, and thus are more promising for the industrial manufacture of PCNs. There are abundant choices of activation agents for chemical activation, including alkaline metal hydroxides (KOH, NaOH, *etc.*), alkaline metal carbonates/bicarbonates (K_2CO_3, Na_2CO_3, $KHCO_3$, $NaHCO_3$, *etc.*), metal chlorides ($ZnCl_2$, $CaCl_2$, *etc.*) and oxidative acids (HNO_3, H_2SO_4, H_3PO_4).[74–84] Among them, KOH is the most powerful activation agent and the activation mechanism can be expressed as outlined below:[11]

$$6KOH + 2C \rightarrow 2K + 3H_2 + 2K_2CO_3 \quad (4)$$

$$K + KOH \rightarrow K_2O + H_2 \quad (5)$$

$$K_2O + CO_2 \rightarrow K_2CO_3 \quad (6)$$

$$K_2CO_3 + 2C \rightarrow 2K + 3CO \quad (7)$$

$$K_2O + C \rightarrow 2K + CO \quad (8)$$

Normally, PCNs obtained from chemical activation possess high SSAs ranging from 500 to 3600 $m^2\ g^{-1}$.[11,85–91] Salt activation agents, such as $ZnCl_2$, generate PCNs with a lower SSA.[92–94] Due to the strong corrosive effect, high cost and high consumption of KOH, KOH activation has limited application for industrial production.[95] Salt activation agents, such as $ZnCl_2$, generate PCNs with lower SSAs that are also corrosive. Furthermore, the high consumption of these agents results in severe contamination, making the development of green and efficient chemical activation agents an urgent task.[11,95,96] Recently, organic potassium salts (OPSs) were explored for the synthesis of PCNs with various morphologies (Fig. 2).[97–101] Compared to KOH, the OPSs and their intermediate products ($KHCO_3$, K_2CO_3, K_2O, K, *etc.*) show much lower corrosion to facilities and require a lower dosage in the activation process. In some cases, OPSs could even serve as the carbon source,

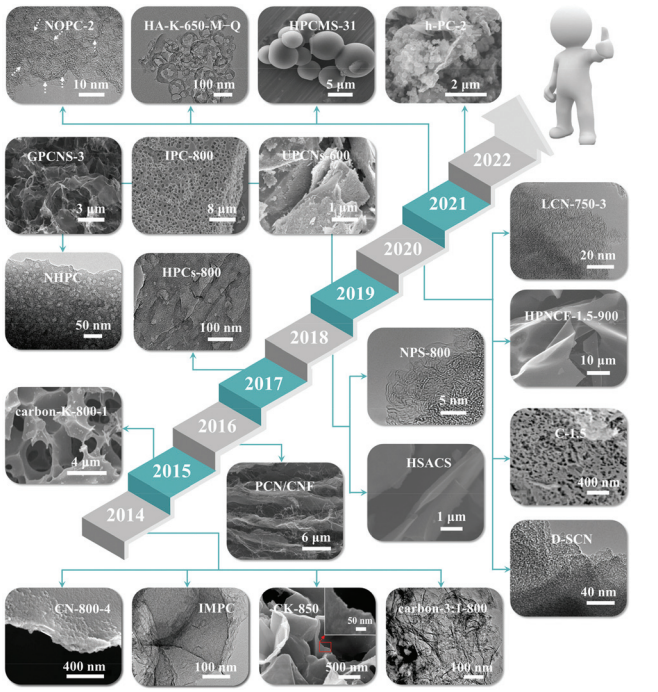

Fig. 2 A brief timeline of porous carbon materials produced from various organic potassium salts and other reagents: CN-800-4 from potassium gluconate and melamine,[52] IMPC from poly(acrylamide-*co*-acrylic acid) potassium salt,[53] CK-850 from potassium citrate,[54] carbon-3 : 1-800 from potassium biphthalate and magnesium powder,[55] carbon-K-800-1 from potassium tartrate,[56] PCN/CNF from potassium citrate and bacterial cellulose,[57] HPCs-800 from potassium acetate and resol,[58] NPS-800 from K-MOF(1),[59] HSACS from EDTA-2K,[60] UPCNs-600 from potassium benzoate,[61] IPC-800 from potassium alginate,[62] GPCNS-3 from potassium formate and pink bark,[63] NHPC from potassium humate and manganous nitrate,[64] LCN-750-3 from potassium phthalimide,[65] HPNCF-1.5-900 from potassium histidine,[66] C-1.5 from potassium oxalate and cornstalk,[67] D-SCN from potassium benzoate and pitch,[68] NOPC-2 from potassium citrate and g-C_3N_4,[69] HA-K-650-M-Q from potassium humate,[70] HPCMS-31 from potassium oxalate, $CaCl_2$ and cassava starch,[71] h-PC-2 from potassium citrate, petroleum asphalt and g-C_3N_4.[72] Reproduced with permission from refs. 52–72. Copyright 2014, 2014, Royal Society of Chemistry; Copyright 2014, American Chemical Society; Copyright 2014, Royal Society of Chemistry; Copyright 2015, 2016, 2017, Elsevier; Copyright 2018, 2018, Wiley; Copyright 2019, 2019, Elsevier; Copyright 2019, American Chemical Society; Copyright 2019, 2020, Elsevier; Copyright 2020, Springer; Copyright 2020, Royal Society of Chemistry; Copyright 2020, 2020, 2021, 2021, 2022, Elsevier.

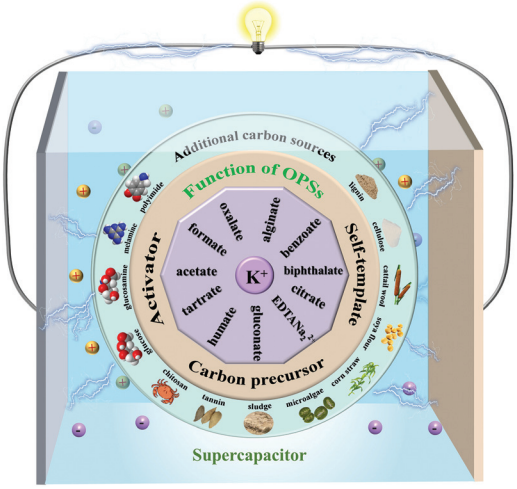

Fig. 3 Schematic of OPSs involved in the synthesis of PCMs and their application in supercapacitors.

template and activation agent simultaneously (Fig. 3).[102–109] In spite of their relatively low content, the intermediate products could be uniformly dispersed within the organic matrix at a molecular level, enabling an effective activation process.[110–112] The organic matrix and its derived carbon matrix will confine the growth of inorganic intermediate products, resulting in the formation of highly micro-/mesoporous carbonaceous products.[52,69,113] In this way, PCNs with a large SSA can be synthesized in one simple step without using large amounts of corrosive chemicals. Organic salts are emerging as versatile precursors in the design of PCNs with special textural properties at the molecular level.[114–122] Compared to other organic salts, OPSs show advantages in performing an activation function and facilitating the template removal process.[66,105,123–127] The *in situ* formed nanosized potassium bicarbonate, potassium carbonate and potassium oxide could serve as effective activation agents and templates for generating massive micro-/meso-pores, which greatly surpassed their counterparts derived from organic salts of Li, Na, Mg, Ca, Al, Zn, *etc*.[128–131] Moreover, the intermediate potassium species could be removed easily by water.[132] While the graphitic carbon layer encapsulating metal nanoparticles derived from organic salts of Fe, Co, Ni, Cu, *etc*., are hard to completely removed, even upon treatment with strong acids. Therefore, OPSs are good choices for the facile and green production of PCNs.

2. Factors influencing the capacitance performance of PCNs

The energy storage mechanism of PCN-based supercapacitors is mainly based on physical charge accumulation at the electrolyte/electrode interface, known as electrochemical double-layer capacitance (EDLC).[133–135] Heteroatom doping could contribute appreciable pseudocapacitance to the total capacitance.[136,137] Also, the capacitance performance of PCNs is greatly influenced by the pore structure and electrical conductivity, which are discussed next.

2.1 The influence of pore structure on the capacitance performance of PCNs

Theoretically, the capacitance of PCNs is directly related to the electrolyte wetted surface area. Typically, increasing the SSA and V_t of PCNs can effectively boost charge accumulation at the electrical double layer formed at the interface of electrode/electrolyte, thus contributing to a larger EDLC.[2] However, some research revealed that ultrahigh SSAs led to a declining volumetric capacitance due to a relatively lower packing density.[138] Hence, good control of the pore size to maximize the ion-accessible surface area and minimize the dead volume is of great importance. Experimental and theoretical studies confirmed that the maximum capacitance could be achieved when the pore size (mainly micropores) of PCNs well matched the size of cations/anions in the liquid electrolytes,[139,140] which was favorable for the formation of the electrical double layer. However, a high capacitance can only be acquired at a low or moderate charge–discharge rate due to a slow ion desolvation and diffusion process in sub-nanometer micropores, which restricts the rate capability and power density.[141] This issue can be resolved by introducing meso-/macropores into microporous PCNs since the macropores can serve as electrolyte reservoirs to shorten the ion transport pathways and mesopores are beneficial for accelerating ion diffusion, contributing to a high capacitance retention at large charging/discharging current densities.[142] On account of this, it is vital to control the ratio of micro-/meso-/macropores in PCNs to achieve a high specific capacitance, good rate performance and satisfactory power density performance.

2.2 The influence of electrical conductivity on the capacitance performance of PCNs

Besides pore structure, electrical conductivity is also an essential factor affecting the capacitance performance of PCNs, especially the rate performance.[143–145] The electrical conductivity of PCNs can be enhanced by increasing the pyrolysis temperature or introducing graphitization catalysts.[146–150] However, the specific capacitance may decrease with an increase of the pyrolysis temperature due to the decreased content of heteroatoms, which leads to a hydrophobic surface on the PCNs and decreased SSA due to the conversion of micropores into mesopores at higher temperature.[151–153] Adding conductive agents is another effective approach to enhance the electrical conductivity of PCNs. Graphene quantum dots, carbon nanotubes (CNTs), graphene nanosheets (GNSs), and Ag nanowires have been demonstrated to have enhanced capacitance performance.[154–158] The addition of CNTs and GNSs not only enhances the electrical conductivity of PCNs, but also benefits the assembly of flexible electrode materials.[158–161]

2.3 The influence of heteroatom doping on the capacitance performance of PCNs

Heteroatom doping, which can modify the surface chemistry of PCNS, proved to be another effective approach to enhance the capacitance performance of PCNs.[17,46,162–165] Without sacrificing the SSA, heteroatoms (B, N, F, O, S Si and P) are capable of generating functional groups on the carbon surface to induce Faradaic reactions and produce pseudocapacitance. Take commonly used N doping as an example, it is validated that the negatively charged pyrrolic and pyridinic N serve as faradaic sites for pseudocapacitance, whereas the positively charged graphitic N and pyridinic N oxide can enhance the electrical conductivity of PCNs.[166–168] B doping is also revealed to induce an uneven charge distribution for faster charge transfer.[169,170] Compared to single atom doping, multiple doping could generate an enhanced effect by facilitating electron transport.[171–174] Surface oxygen functional groups are also effective and have been confirmed to contribute up to 30% of the total capacitance of PCNs in alkaline solution.[175] The introduction of heteroatoms could also enhance the wettability of the carbon surface, contributing to an enhanced effective surface area and electrical double-layer capacitance.[162,176,177]

3. Porosity development mechanisms for OPS-based synthesis of PCNs

The function of OPSs greatly relies on the structure of the anions. If the oxygen content in the organic anion is higher than the carbon content, OPSs would be converted into potassium carbonate upon pyrolysis at high temperature.[178] The formed potassium carbonate would then serve as the activation agent. In this case, OPSs are the precursor of the activation agent. Potassium formate and potassium oxalate fall into this category.[63,67,179,180]

When the oxygen content is much lower than the carbon content in organic anions, carbonaceous products would be obtained along with potassium carbonate through the direct pyrolysis of OPSs.[103,181,182] The formed potassium carbonate not only acts as an activation agent but also acts as template. In this case, the OPSs serve as the precursors of carbon, activation agents, and templates simultaneously. Most OPSs including but not limited to potassium acetate/citrate/tartrate/gluconate/humate/benzoate/biphthalate/alginate fall into this category.[65,66,70,183–187] During the pyrolysis process, molecularly dispersed potassium carbonate is formed *in situ* and nanopores are generated effectively. In this way, PCNs with SSAs of 1410 m^2 g^{-1} to 3179 m^2 g^{-1} can be obtained by only one simple step, avoiding the introduction of large amounts of external corrosive chemical agents.[60,110] The pyrolysis process of those OPSs shows certain analogies to the activation process of KOH. At relatively low temperatures (*i.e.*, 500–650 °C), the formation of K_2CO_3 takes place.[104,110] At higher temperatures, K_2CO_3 decomposes ($K_2CO_3 \rightarrow K_2O + CO_2$) and the evolved CO_2 then reacts with the carbon matrix ($C + CO_2 \rightarrow 2\ CO$), generating micropores.[188–191] Simultaneously, metallic potassium is generated from the reduction of potassium oxide by the carbon matrix (eqn (8)). Metallic potassium plays a vital role in the formation of additional porosity because its vapor is intercalated between the graphene layers, resulting in swelling and disruption of the carbon microstructure.[110,178] These reactions synergistically lead to the generation of PCNs.

Generally, the yields of PCNs obtained from the direct pyrolysis of OPSs are relatively low. Hence, additional carbon sources are always introduced into the process. In those cases, OPSs serve primarily as the activation agents. The following subsections are organized according to the function of OPSs in the synthesis of PCNs in the order of activation agents, primary carbon sources, activation agents and partial carbon sources.

4. Capacitance performance of PCNs synthesized with OPSs as the activation agent

Usually, oxygen-rich OPSs such as potassium formate, potassium acetate and potassium oxalate are decomposed and converted into potassium carbonate, carbon dioxide and water at elevated temperature. Therefore, these OPSs often serve as the activation agents to generate PCNs.[192–196] As listed in Table 1, PCNs could be synthesized from various precursors by using oxygen-rich OPSs as the activation agent. Wang *et al.* synthesized graphene-like porous carbon nanosheets (GPCNS-X) from pine bark with potassium formate as the activation agent for a nonaqueous supercapacitor (Fig. 4a).[63] The effect of the weight ratio between potassium formate and pine bark on the morphology and microstructure of the resulting products was investigated. It was found that all the products exhibited a wrinkled nanosheet structure (Fig. 4b) in the range of 2 : 1 to 4 : 1 but the size and thickness decreased with an increase of the ratio. The porosity of GPCNS-X samples was dominated by micropores and mesopores as confirmed by the type I and type IV characteristics of the nitrogen adsorption–desorption isotherms (Fig. 4c). The SSA and V_t increased from 1627.5 m^2 g^{-1} to 2085.6 m^2 g^{-1}, and 1.08 cm^3 g^{-1} to 1.59 cm^3 g^{-1}, respectively, with an increase of the potassium formate content. Micropores decrease and mesopores increase with an increase of the ratio and the average pore size is increased from 1.73 nm to 2.98 nm. The capacitance performance was evaluated by using a symmetric coin cell in 1 M $TEABF_4$/AN electrolyte. Among the three samples, GPCNS-3 synthesized with a ratio of 3 : 1 exhibited the best rate performance of 128.1 F g^{-1} at 1 A g^{-1} and retained 97.8 F g^{-1} at 40 A g^{-1} (Fig. 4d). GPCNS-3 also showed good stability with a capacitance retention of 93.9% after 10 000 cycles at 5 A g^{-1} (Fig. 4e). Moreover, the maximum energy density (E_{max}) and power density (P_{max}) of GPCNS-3 reached 32.4 W h kg^{-1} and 30.375 kW kg^{-1}, respectively.

Table 1 Pore structure and capacitance performance of PCNs prepared from various carbon sources with OPSs as the activation agent

PCNs	OPS	Other reagents	SSA (m^2 g^{-1})	V_t (cm^3 g^{-1})	V_m (cm^3 g^{-1})	d (nm)	Electrolyte	C_{sp} (F g^{-1})	E_{max} (W h kg^{-1})	P_{max} (kW kg^{-1})	Cycle life	Rate performance	Ref.
GPCNS	Potassium formate	Pine bark powders	1816.3	1.16	1.16	2.49	1 M $TEABF_4$/AN	128.1 F g^{-1} at 1 A g^{-1}	32.4	30.375	93.9%, 10 000, 5 A g^{-1}	97.8 F g^{-1} at 40 A g^{-1}	63
HPCs-800	Potassium acetate	Resol	1201	1.09	1.09	—	7 M KOH	222 F g^{-1} at 0.05 A g^{-1}, (2E)	—	—	—	73% at 20 A g^{-1}	58
NPC-800	Potassium acetate	Phenol-urea-formaldehyde resins	1571	0.76	0.76	1.94	7 M KOH	260 F g^{-1} at 0.05 A g^{-1} (2E)	8.21	6.59	96.6%, 5000, 2 A g^{-1}	73% at 20 A g^{-1}	197
HPC-15	Potassium acetate	Freeze-dried bean curd	2180	1.18	1.18	2.17	6 M KOH	284 F g^{-1} at 0.1 A g^{-1}, (2E)	9.9	10	—	80% at 10 A g^{-1}	198
PC-5	Potassium acetate	Chitosan	2336.2	1.13	1.13	1.93	6 M KOH	183.3 F g^{-1} at 1 A g^{-1}	—	—	—	75.8% at 10 A g^{-1}	199
PC-2	Potassium acetate	Chitosan, K_2CO_3	2289	1.21	1.21	2.11	6 M KOH	374.4 F g^{-1} at 1 A g^{-1}	—	—	95.9%, 10 000	76.4% at 10 A g^{-1}	199
HPCMS-31	Potassium oxalate	Hydrochar of cassava starch, $CaCl_2$	1668	0.61	0.61	—	6 M KOH	286 F g^{-1} at 0.5 A g^{-1}	—	—	98%, 20 000, 20 A g^{-1}	71% at 50 A g^{-1}	71
ASC-700	Potassium oxalate	Semen cassiae seeds	1123.8	0.64	0.64	—	1 M H_2SO_4	401 F g^{-1} at 1 A g^{-1}	12.01 (2E)	10.2 (2E)	94.5%, 10 000, 5 A g^{-1}	275 F g^{-1} at 30 A g^{-1}	200
2D-NPC	Potassium oxalate	Glucose, melamine	1730	1.51	1.51	—	6 M KOH	523 F g^{-1} at 0.5 A g^{-1}	—	—	100%, 10 000, 10 A g^{-1}	347 F g^{-1} at 20 A g^{-1}	201

1 M $TEABF_4$/AN, 1 M of tetraethylammonium tetrafluoroborate ($TEABF_4$) in acetonitrile (AN); V_m, total micropore volume; d, mean pore size; 2E, two-electrode symmetric configuration.

Zhang *et al.* explored the capacitance performance of hierarchical porous carbons (HPCs) synthesized by the pyrolysis of a mixture of resol and potassium acetate (1 : 3, w/w) at 600 °C to 800 °C.[58] The volume of mesopores and macropores increased dramatically with increasing pyrolysis temperature. The SSA and V_t increased from 897 m^2 g^{-1} and 0.43 cm^3 g^{-1} for HPCs-600 to 1201 m^2 g^{-1} and 1.09 cm^3 g^{-1} for HPCs-800. Potassium acetate plays a key role in the formation of a honeycomb-like porous network structure. The control sample synthesized without potassium acetate showed a relatively smooth surface with no obvious pores. The C_{sp} of HPCs-700 and HPCs-800 reached 226 F g^{-1} and 222 F g^{-1} at 0.05 A g^{-1}; these values were much larger than that of HPCs-600 (186 F g^{-1}). HPCs-800 showed the best rate performance with a capacitance retention of 73.0% at 20 A g^{-1}. To improve the capacitance performance of HPCs, urea was introduced into the synthesis of the carbon source, resulting in a phenol–urea–formaldehyde resin prepolymer (Fig. 5a).[197] A series of nitrogen-doped porous carbon (NPCs) were obtained by the pyrolysis of the resin prepolymer and potassium acetate at 700 °C to 900 °C. From the pore size distribution curves (Fig. 5b), one could tell that the porosity of NPC-700 was dominated by micropores while larger mesopores gradually increased with an increase of the pyrolysis temperature. The SSA and V_t increased from 791 m^2 g^{-1} and 0.37 cm^3 g^{-1} for NPC-700 to 1946 m^2 g^{-1} and 0.98 cm^3 g^{-1} for NPC-900. The nitrogen content decreased from 6.37% for NPC-700 to 1.79% for NPC-900. The charge and discharge curves of NPC-800 at current densities ranging from 0.5 A g^{-1} to 20 A g^{-1} (Fig. 5c) presented approximately symmetrical triangular shapes, suggesting almost ideal EDLC behavior and good electrochemical reversibility of NPC-800. The C_{sp} reached 312 F g^{-1}, 296 F g^{-1} and 259 F g^{-1} at 0.5 A g^{-1} for NPC-700, NPC-800, and NPC-900, respectively (Fig. 5d). NPC-700 showed the largest C_{sp} at low current density owing to it possessing the highest N content, which contributed substantial pseudocapacitance. However, the capacitance retention ratio increased gradually with an increase of temperature due to the loss of unstable nitrogen species at high temperature resulting in a reduction of the pseudocapacitance. On the other hand, the increase in EDLC contribution will contribute to an enhanced rate performance. The capacitance retention ratios at 20 A g^{-1} of NPC-700, NPC-800 and NPC-900 in a symmetric supercapacitor device were 61%, 73% and 74%, respectively. NPC-800 also showed good stability with a capacitance retention of 96.5% after 5000 cycles at 2 A g^{-1} (Fig. 5e).

Li and coworkers synthesized a series of N-doped hierarchical porous carbon materials by pyrolysis of a mixture of bean curd and potassium acetate at 750 °C.[198] The porosity of PCNs increased with increasing mass percentage of potassium acetate. The control sample (HPC-0) and the sample prepared from 5% potassium acetate (HPC-5) displayed a rather dense structure while the ones pyrolyzed from 15% and 20% potassium acetate (HPC-15 and HPC-20) exhibited a honeycomb-like structure. The SSA of HPCs increased from 89 m^2 g^{-1} to 2180 m^2 g^{-1} as the mass fraction of potassium acetate increased from 5% to 15% and decreased to 1672 m^2 g^{-1} when

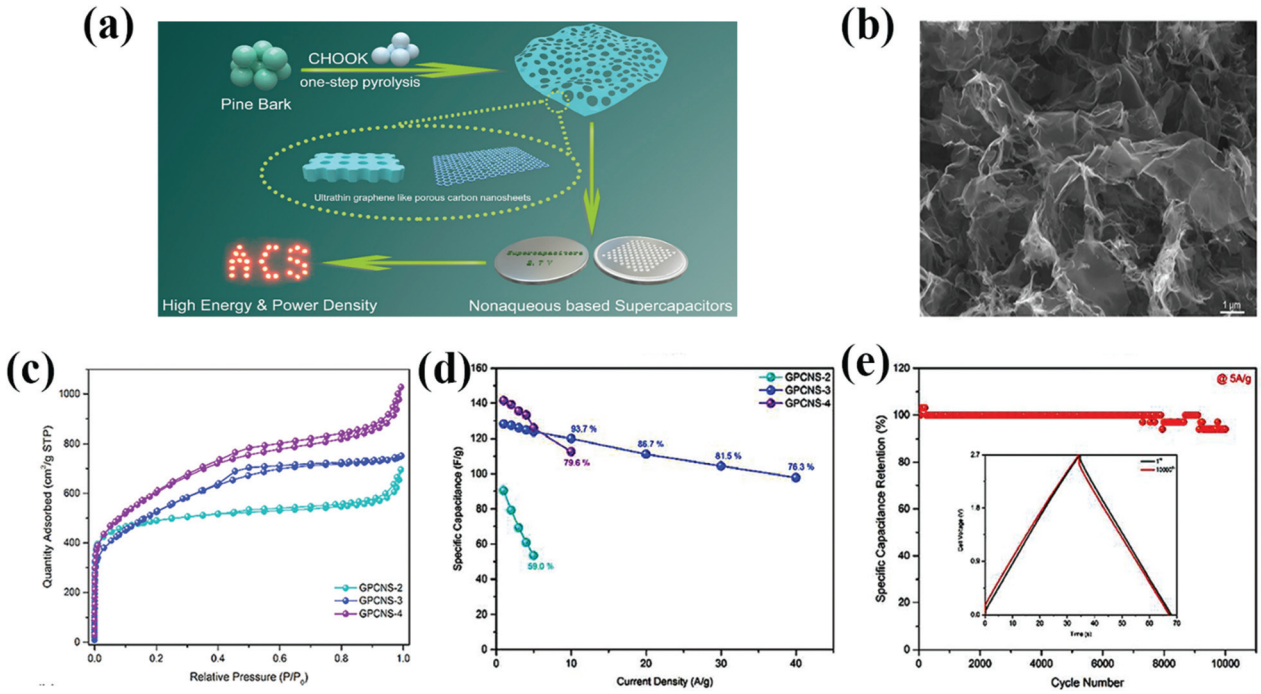

Fig. 4 (a) Schematic diagram demonstrating the synthetic process and application of GPCNSs in supercapacitors. (b) FESEM image showing the thin layer structure of GPCNS-3. (c) Nitrogen adsorption–desorption isotherms of GPCNS samples. (d) Specific capacitance of GPCNS samples at different current densities. (e) Cycling stability test of GPCNS-3 at 5 A g^{-1}; inset shows the charge/discharge curves after the initial and 10 000th cycles. Reproduced with permission from ref. 63. Copyright 2019, American Chemical Society.

the dosage of potassium acetate was 20%. The variation tendency of the microporous surface area, mesoporous surface area, V_t and V_m is similar. HPC-15 showed the highest C_{sp} of 355 F g^{-1} at 0.1 A g^{-1} in 1 M H_2SO_4 electrolyte and 284 F g^{-1} at 0.1 A g^{-1} in 6 M KOH electrolyte among all the samples. The E_{max} and P_{max} of HPC-15 reached 12 W h kg^{-1} and 10 kW kg^{-1} in 1 M H_2SO_4 electrolyte.

Qiao *et al.* reported a nitrogen-doped hierarchical porous carbon synthesized by pyrolyzing a mixture of chitosan, potassium carbonate, and potassium acetate at 800 °C.[199] It was found that the PCNs produced from the mixture of potassium carbonate and potassium acetate showed enhanced porosity compared with the ones synthesized from a single potassium salt. The porosity of the three PCNs synthesized from the mixture of potassium carbonate and potassium acetate with molar ratios of 0.5 : 1 to 1.5 : 1 was dominated by micropores (77.7% to 97.3%) with a total SSA higher than 2200 m^2 g^{-1} and V_t higher than 0.9 cm^3 g^{-1}. The PCNs synthesized from dual potassium salts showed a much better capacitance performance than those from a single potassium salt. PC-2 obtained from potassium carbonate and potassium acetate with a molar ratio of 0.5 : 1 exhibited a C_{sp} of 374.4 F g^{-1} at 1 A g^{-1}, which was the best capacitance performance among all the PCNs. The samples produced only from potassium carbonate and potassium acetate showed C_{sp} values of 201.4 F g^{-1} and 148.2 F g^{-1}, respectively. All the PCNs exhibited high capacitance retention above 75% at a current density of 10 A g^{-1}; this was attributed to the hierarchical pore structure.

Potassium oxalate is another effective activation agent for preparing high capacitance PCNs. Zheng's group reported the synthesis of hierarchically porous carbon microspheres (HPCMSs) for supercapacitor with cassava starch as the carbon precursor and potassium oxalate monohydrate and calcium chloride as the activators.[71] The yield of HPCMSs reached ~50% (to hydrochar intermediates), which was much higher than that for PCNs obtained by KOH activation (10–15%). The HPCMSs showed a nice spherical shape with sizes of 4–6 μm. The SSA values of HPCMSs were all above 1200 m^2 g^{-1}. Pore structure analysis indicated that calcium chloride was effective at generating meso-/macro-pores. The HPCMS synthesized from hydrothermal products of cassava starch, potassium oxalate and calcium chloride at a mass ratio of 1 : 3 : 1 showed the best capacitance performance of all the samples with a C_{sp} of 286 F g^{-1} at 0.5 A g^{-1} and retained 71% capacitance at 50 A g^{-1} in 6 M KOH electrolyte.

A series of sponge-like hierarchical PCNs were synthesized by the pyrolysis of potassium oxalate impregnated semen cassiae at 600 °C to 800 °C.[200] Potassium oxalate could effectively introduce porous structures into PCNs. ASC-700 synthesized at 700 °C exhibited the largest SSA of 1123.8 m^2 g^{-1} of the three activated samples, while the control sample produced without potassium oxalate showed quite a low SSA of 10.2 m^2 g^{-1}. The thickness of the carbon layers gradually decreased as the calcination temperature increased. ASC-700 showed the best capacitance performance with a high C_{sp} of 401 F g^{-1} at 1 A g^{-1} and retained 275 F g^{-1} at 30 A g^{-1} in 1 M H_2SO_4 electrolyte.

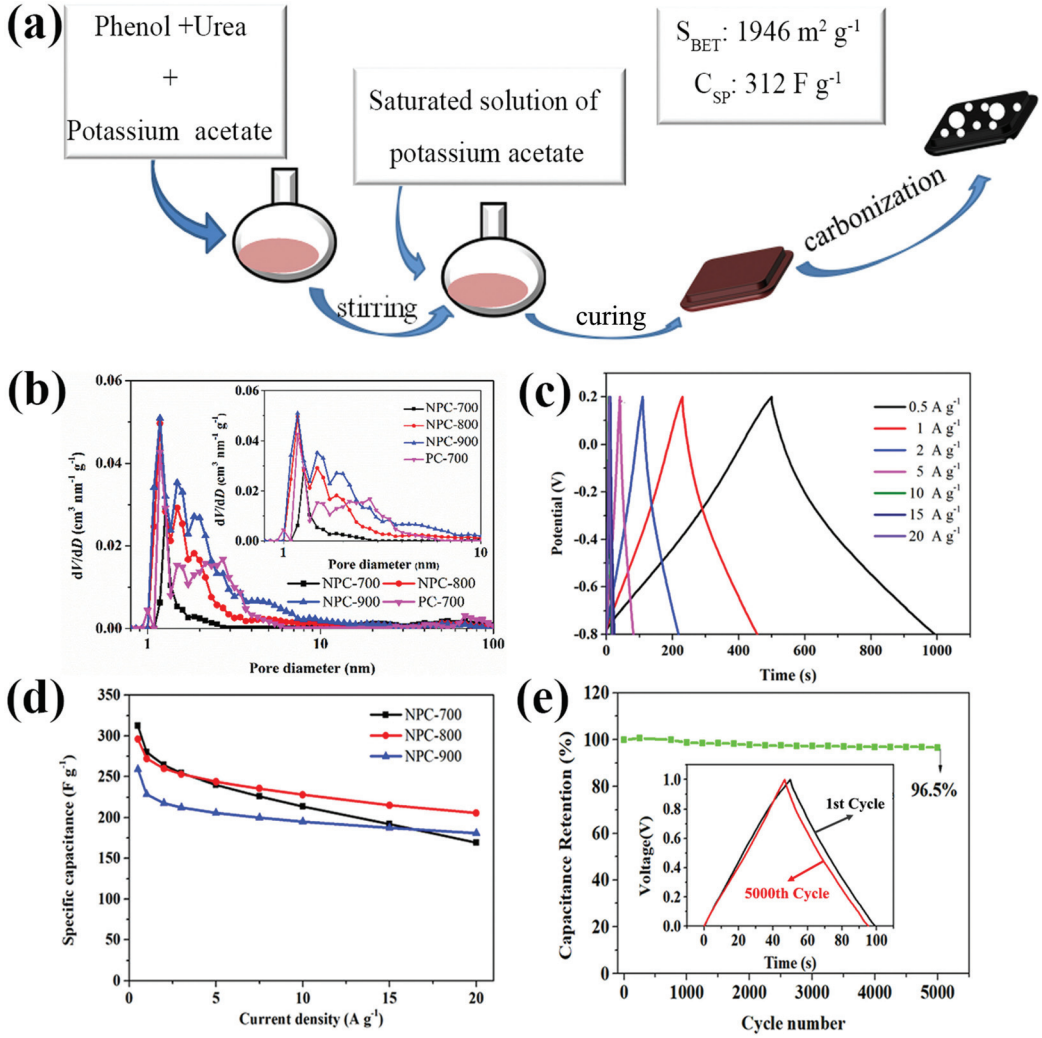

Fig. 5 (a) Schematic diagram demonstrating the fabrication process for NPC. (b) Pore size distribution curves of NPC samples. (c) Charge/discharge curves of NPC-800 at varied current densities. (d) Specific capacitance of NPC samples at different current densities. (e) Cycling stability of NPC-800 at 2.0 A g^{-1} in a two-electrode system. Reproduced with permission from ref. 197. Copyright 2018, Elsevier.

Two-dimensional N-doped hierarchical porous carbon nanosheets (2D-NPC) were synthesized using potassium oxalate as the activating agent, glucose as the carbon source and melamine as the nitrogen source and blowing agent.[201] Melamine plays a decisive role in the formation of a sheetlike structure while potassium oxalate generates a lot of meso-/macro-pores on the nanosheets. As shown in Fig. 6a, the carbonaceous products produced from different recipes exhibited varied morphologies. Large brick-like carbon particles (G-C) were obtained from the direct carbonization of glucose. Nitrogen-doped carbon (G-NC) with a sheetlike structure was obtained from the pyrolysis of a mixture of glucose and melamine owing to the blowing effect of melamine. Porous carbon (G-PC) particles exhibited a fragmented bulk morphology along with some exfoliated thin carbon nanosheets, which were obtained from the pyrolysis of a mixture of glucose and potassium oxalate. 2D-NPC showed a thin sheet structure with big pores on the edges generated from the pyrolysis of a mixture of glucose, melamine and potassium oxalate. The SSA and V_t increased in the order of G-C < G-NC < G-PC < 2D-NPC with 106 m^2 g^{-1} and 0.09 cm^3 g^{-1} for G-C and 1730 m^2 g^{-1} and 1.51 cm^3 g^{-1} for 2D-NPC. From the pore size distribution curves (Fig. 6b), it could be observed that, once melamine was introduced, the pore size of 2D-NPC was extended to 2–4 nm in comparison with that of G-PC (mainly micropores). The formation mechanism of 2D-NPC based on the synergistic effect of melamine and potassium oxalate is depicted in Fig. 6c. Potassium oxalate accelerated the dehydration and polymerization of glucose. The carbon precursor was exfoliated into nanosheets by the gas released through the decomposition of melamine. Potassium carbonate was formed from the decomposition of potassium oxalate and etched the 2D carbon nanosheets, resulting in a high amount of meso-/macropores (64%). The nitrogen element from the decomposition of melamine was incorporated into the carbon structure simultaneously. The CV curve of 2D-NPC exhibited a quasi-rectangu-

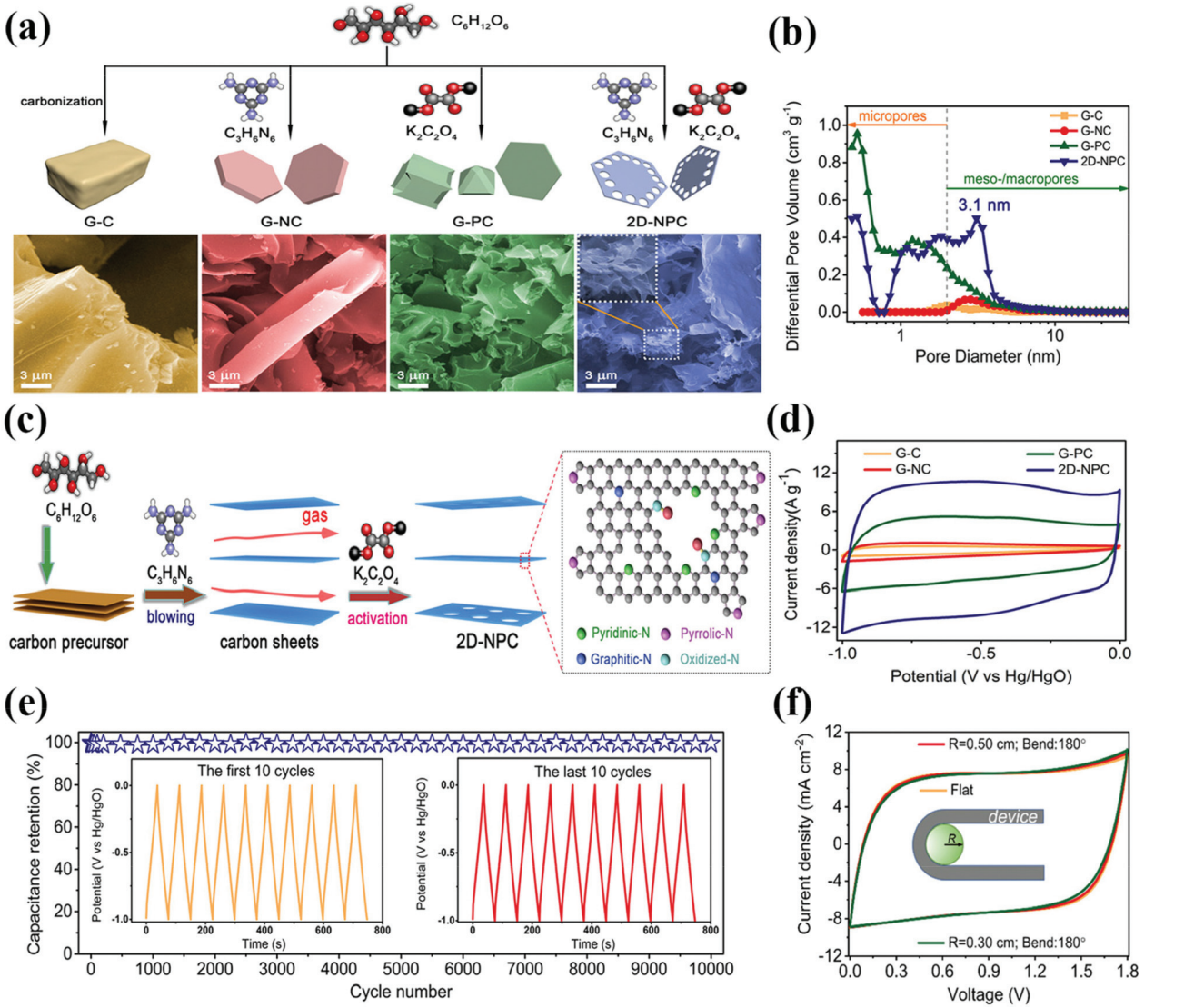

Fig. 6 (a) Synthesis of samples *via* a one-step pyrolysis process and corresponding SEM images of G-C, G-NC, G-PC, and 2D-NPC. (b) Pore size distribution curves of porous carbon samples. (c) Illustration of the formation process of 2D-NPC. (d) CV curves at 20 mV s^{-1}. (e) Cycling stability of 2D-NPC at 10 A g^{-1}. (f) CV curves of the flexible supercapacitor device at varied bending radii in the PVA/LiCl gel electrolyte. Reproduced with permission from ref. 201. Copyright 2020, American Chemical Society.

lar shape, indicating the dominant role of EDLC (Fig. 6d). The redox reaction of oxygen/nitrogen dopants caused the deformation of the CV curve. 2D-NPC exhibited the largest capacitance, as depicted by the largest CV integral area. The C_{sp} of 2D-NPC reached 523 F g^{-1} at 0.5 A g^{-1} which was much larger than that of the sample derived from glucose and melamine (49 F g^{-1}) and the sample from glucose and potassium oxalate (294 F g^{-1}). 2D-NPC also exhibited a good rate performance with 347 F g^{-1} at 20 A g^{-1}, and good stability with no capacitance decay after 10 000 cycles at 10 A g^{-1} (Fig. 6e). A supercapacitor based on 2D-NPC exhibited good flexibility as the CV curves showed little changes between the flat and the bent state (Fig. 6f).

Table 1 summarizes the use of potassium formate, potassium acetate, and potassium oxalate as efficient activation agents for the synthesis of PCNs from various carbon sources. Compared to KOH, the OPSs are less corrosive with low toxicity, while their prices are a little higher than that of KOH. The dosage of the OPSs used for activation is always more than the mass of carbon precursor. Potassium formate is more efficient at producing carbon nanosheets while potassium acetate and potassium oxalate tend to generate porous networks. Generally, the porous structure of PCNs could be tuned by varying the mass ratio of those OPSs and the carbon precursor and changing the pyrolysis temperature. The pores of PCNs synthesized with a low mass ratio of OPSs to the carbon source or carbonized at relatively low temperature (*e.g.* <800 °C) are always dominated by micropores. Conversely, hierarchical PCNs will be obtained if high mass ratio of OPSs to the carbon source or higher carbonization temperature is selected.

Irregular blocky microparticles are obtained in the absence of OPSs. The SSA and V_t surpass 2000 $m^2 g^{-1}$ and 1.1 $cm^3 g^{-1}$ for the optimal sample. Blocky carbon materials with SSAs of 0.7 $m^2 g^{-1}$ to 106 $m^2 g^{-1}$ are obtained without OPSs as the activation agents.[198,200,201] Compared to the C_{sp} of control samples (23.5 F g^{-1} to 28 F g^{-1}) prepared without OPSs,[200,201] the C_{sp} of those samples synthesized with the addition of potassium citrate shows greatly enhanced capacitance performance (183.3 F g^{-1} to 523 F g^{-1}).[199,201]

5. Capacitance performance of PCNs synthesized with OPSs as the primary carbon sources

Potassium citrate is the most widely used OPS for the synthesis of PCNs because it possesses the largest carbon yield among common OPSs.[60] As summarized in Table 2, various PCNs could be synthesized from potassium citrate. Sevilla *et al.* did pioneering research in the design of PCNs with carbon-rich OPSs.[110] They reported the facile synthesis of highly porous carbon from organic salts of Na, K or Ca (gluconates, alginates and citrates) by heat-treatment at 800 °C and an acid washing process.[110] The morphology of the resulting carbon materials varied from irregular particles to vesiculated particles, sponge-like particles, and nanosheets, greatly depending on the organic salts used. The SSAs span from 650 $m^2 g^{-1}$ for sodium citrate-derived carbon to 1960 $m^2 g^{-1}$ for potassium citrate-derived carbon. For the K salt-derived carbon materials, the pores were basically made up of micropores (~75% V_t) together with a small fraction of mesopores. The pores of sodium gluconate and calcium citrate-derived carbon materials were dominated by mesopores. The mesoporous carbon nanosheets derived from sodium gluconate showed uniform mesopores of around 12 nm. The calcium citrate-derived mesoporous carbon displayed textural properties with a uniform mesopore size of ~10 nm, a high SSA of 1510 $m^2 g^{-1}$, and a large pore volume of 2.6 $cm^3 g^{-1}$. The porosity formation process was discussed. For the K and Na salts, carbonates were formed at 500–650 °C, while oxides were obtained at higher temperatures, which were finally reduced to metallic Na and K by the carbon matrix. Micropores were generated from the activation process of CO_2 (evolved from the decomposition of carbonates) and the intercalation effect of Na and K. Compared to their counterparts derived from K and Na salts, the carbon materials obtained from Ca salts possessed a larger portion of mesopores; this was attributed to the template effect of CaO.

The carbon nanosheets derived from potassium citrate are of special interest for supercapacitors considering the short diffusional paths, which contribute to enhanced ion-transport kinetics.

Hence, Sevilla *et al.* further explored the capacitance performance of potassium citrate-derived carbon materials in 1 M $TEABF_4$/AN electrolyte.[54] Carbon particles assembled from interconnected microporous carbon nanosheets (PCNS) with

Table 2 Pore structure and capacitance performance of potassium citrate derived PCNs

PCNs	Other reagents	SSA ($m^2 g^{-1}$)	V_t ($cm^3 g^{-1}$)	d (nm)	Electrolyte	C_{sp} (F g^{-1})	E_{max} (W h kg^{-1})	P_{max} (kW kg^{-1})	Cycle life	Rate performance	Ref.
CK-850	—	2220	1.11	—	1 M $TEABF_4$/A	150 F g^{-1} at 1 mV s^{-1}	18	17	90%, 10^4 cycles at 10 A g^{-1}	85% at 150 A g^{-1}	54
S-PCN-3	—	727	—	—	6 M KOH	277 F g^{-1} at 1 A g^{-1}	~8.4 (2E)	50 (2E)	98%, 20 000 cycles	144 F g^{-1} at 200 A g^{-1}	111
KN850(8 : 2)	Trisodium citrate dihydrate	1442	0.76	—	6 M KOH	200 F g^{-1} at 5 mV s^{-1}	—	—	90%, 10^4 cycles at 10 A g^{-1}	99 F g^{-1} at 500 mV s^{-1}	112
N-ACN10	MgO nanosheets template, NH_3	1630	—	—	6 M KOH	331 F g^{-1} at 2 mV s^{-1}	—	—	98%, 10 000 cycles	203 F g^{-1} at 5 V s^{-}	202
HPGC-750	Diammonium oxalate monohydrate	2973	1.62	2.18	6 M KOH	322.6 F g^{-1} at 0.5 A g^{-1}	—	—	101.5%, 15 000 cycles at 100 mV s^{-1}	258.4 F g^{-1} at 30 A g^{-1}	147
NMCNS-1	Ammonium citrate	1900	0.95	—	6 M KOH	356 F g^{-1} at 0.5 A g^{-1}	11.8	—	—	238 F g^{-1} at 20 A g^{-1}	203
NOPC-2	g-C_3N_4	2557	1.85	—	6 M KOH	527 F g^{-1} at 1 A g^{-1}	14.5	25	94.3%, 20 000 cycles at 10 A g^{-1}	246 F g^{-1} at 200 A g	69
NS-SHC-8 : 8	Thiourea	209	—	—	1 M H_2SO_4	258.5 F g^{-1} at 0.5 A g^{-1}	—	—	94.4%, 20 000 cycles at 100 mV s^{-1}	206.5 F g^{-1} at 10 A g^{-1}	204

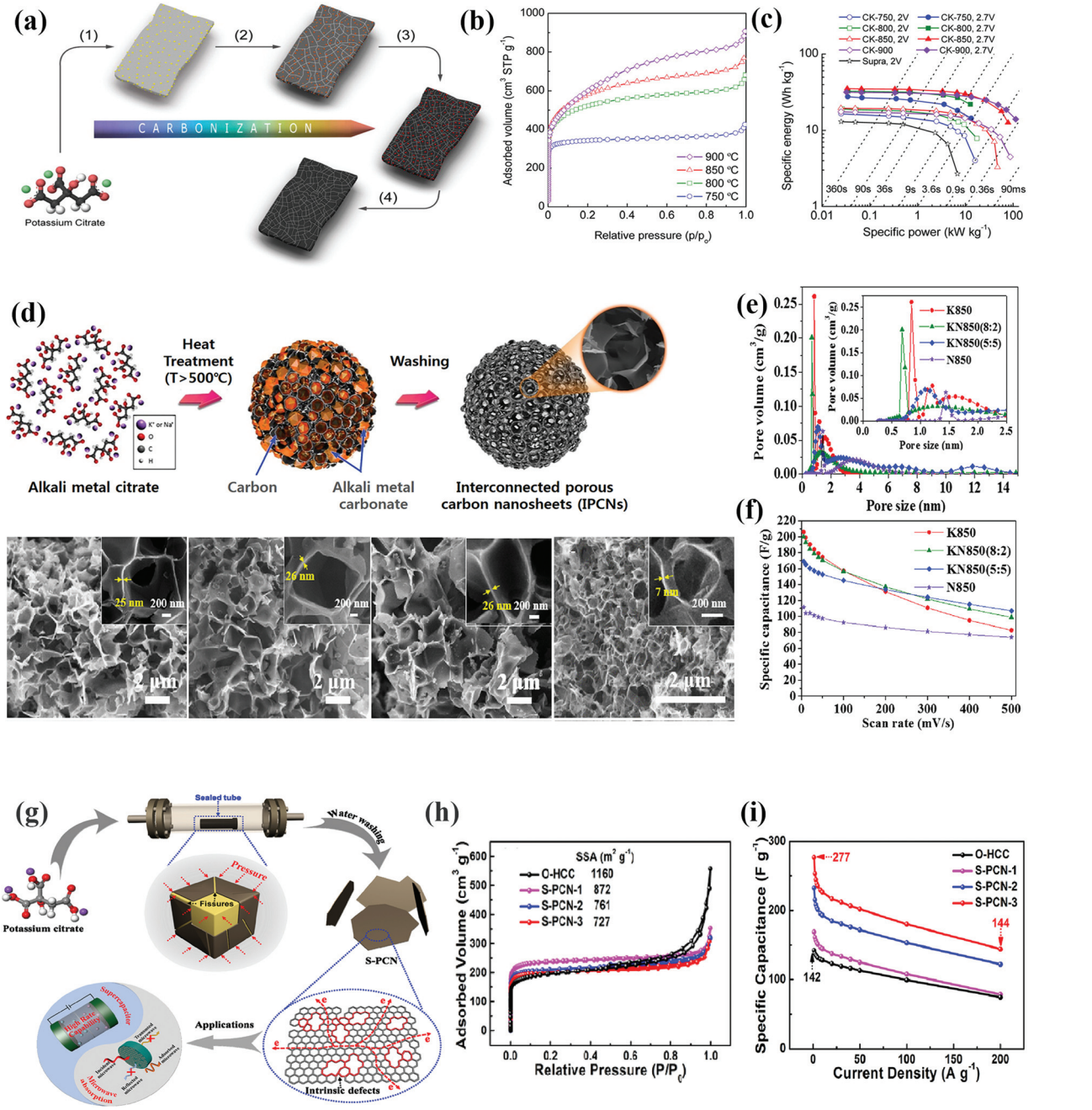

Fig. 7 (a) Schematic diagram demonstrating the preparation of porous carbon nanosheets from potassium citrate. (1) Pyrolysis of potassium citrate and the formation of K_2CO_3; (2) decomposition of K_2CO_3 to K_2O; (3) reduction of K_2O with the formation of metallic K; (4) removal of inorganic potassium compounds. (b) Nitrogen sorption isotherms of PCNS samples obtained by pyrolysis at different temperatures. (c) Ragone plots of the samples in 1 M $TEABF_4$/AN electrolyte. (d) Schematic of the formation mechanism for IPCNs and their corresponding FE-SEM images. From left to right, microporous IPCNs produced from potassium citrate (K850), hierarchical micro-/mesoporous IPCNs derived from a 8 : 2 (w/w) mixture (KN850(8 : 2)) and a 5 : 5 (w/w) mixture (KN850(5 : 5)) of potassium citrate and sodium citrate, and mesoporous IPCNs synthesized from sodium citrate (N850). The insets show magnified images of the corresponding samples. (e) Pore size distribution curves of IPCNs. (f) Specific capacitance of IPCNs at different scan rates. (g) Schematic of the preparation of S-PCN and its dual applications. (h) Nitrogen adsorption–desorption isotherms of samples. (i) Specific capacitance at different current densities. Reproduced with permission from ref. 49, 112 and 111. Copyright 2014, American Chemical Society; Copyright 2018, Elsevier; Copyright 2021, Elsevier.

thicknesses less than 80 nm were obtained by the carbonization of potassium citrate at 750–900 °C (Fig. 7a). Nitrogen sorption isotherms were categorized as type I (Fig. 7b), indicating that the porosity was dominated by micropores. A widening of the isotherms takes place as the carbonization temperature increases from 750 to 900 °C, which implies an enlargement

of the micropore size with an increase of temperature. There are two pore systems in the micropore range. As the carbonization temperature increases from 750 to 900 °C, the main maximum shifts from 0.7 to 0.85 nm, whereas the second pore system is widened from 0.95 nm (750 °C) to 1.6 nm (900 °C). The carbon particles are mainly composed of carbon (>93 at%), with an amount of oxygen (<6.6 at%). The V_t of the carbon particles increased from 0.59 $cm^3\ g^{-1}$ (CK-750, 750 °C sample) to 1.30 $cm^3\ g^{-1}$ (CK-900, 900 °C sample), while the SSA reached a maximum of 2220 $m^2\ g^{-1}$ at 850 °C. The electrical conductivity increased from 1.7 S cm^{-1} to 7.4 S cm^{-1} with an increase of the carbonization temperature. The carbon sample synthesized at 850 °C (CK-850) showed the best capacitance performance among all the samples. The C_{sp} of CK-850 reached a maximum of ~150 F g^{-1} at 1 mV s^{-1} and retained 55% capacitance at a high scan rate of 1 V s^{-1}. CK-850 could reach a high current density of 150 A g^{-1} with only 15% decay. The Ragone plot in Fig. 7c compares the activated carbon Supra and the PCNS samples. The energy density of CK-850 was 18 W h kg^{-1} at 2.5 kW kg^{-1} and retained 12 W h kg^{-1} at 17 kW kg^{-1}, which was much larger than that of Supra (9 W h kg^{-1} at 2.5 kW kg^{-1}). CK-850 also showed good stability with a capacitance retention of 90% after 10 000 cycles at 10 A g^{-1}. The good capacitance performance of CK-850 is attributed to its unique interconnected nanosheet structure, which inhibits the aggregation of carbon nanosheets and facilitates electron transport.

Lee and co-workers also reported the synthesis of interconnected porous carbon nanosheets (IPCNs) from the pyrolysis of alkali metal citrates in a single step and proposed a self-templating mechanism.[112] Microporous, mesoporous, and hierarchical micro/mesoporous IPCNs could be obtained by the carbonization of tripotassium citrate monohydrate, trisodium citrate dihydrate, and their mixtures at 850 °C for 3 h, respectively. The stepwise formation mechanism of IPCN is depicted in Fig. 7d. The potassium carbonate and sodium carbonate formed *in situ* during the pyrolysis process acted not only as activation/etching agents but also as templates for the formation of carbon nanosheets. SEM images showed that the IPCNs derived from different organic salts exhibited different morphologies. The porous carbon nanosheets obtained from potassium citrate and potassium/sodium citrates connected with each other and formed an angular shape, while the carbon nanosheets produced from sodium citrate displayed more rounded corners. The thickness of the carbon nanosheets produced from potassium citrate and potassium/sodium citrates was about 20–50 nm (with an edge length of 500–2000 nm), which was thicker than that of their counterparts derived from sodium citrate (5–10 nm, with an edge length of 100–400 nm). The SSA of potassium citrate derived IPCNs reached 1736 $m^2\ g^{-1}$, which was about 5 times the value of sodium citrate derived IPCNs (361 $m^2\ g^{-1}$). The IPCNs produced from the mixture of potassium citrate and sodium citrate showed an intermediate SSA (1442 $m^2\ g^{-1}$ for 8 : 2 sample, 1261 $m^2\ g^{-1}$ for 5 : 5 sample). The pore size distribution curves in Fig. 7e indicated that the IPCNs exhibited different pore structures. Potassium citrate derived IPCNs were predominantly comprised of micropores while their sodium citrate derived counterparts contained mostly mesopores. The IPCNs derived from mixed citrates contained both micropores and mesopores. The differences in pore size distribution and particle morphology between IPCNs are probably attributed to the differences in the size and morphology of potassium carbonate and sodium carbonate. Pores could also be produced from the volatilization of K/Na generated from carbothermal reduction. The hierarchical micro-/mesoporous IPCNs derived from the mixed citrates showed a better capacitance performance than the ones generated from a single citrate (Fig. 7f). The C_{sp} of KN850(8 : 2) reached 200 F g^{-1} at 5 mV s^{-1} and retained 49% capacitance at 500 mV s^{-1}. The supercapacitor based on KN850(8 : 2) also showed good cyclability without any evident decay after 1000 cycles at 100 mV s^{-1}.

Recently, Hou *et al.* developed a simple strategy to prepare intrinsic defect-rich porous carbon nanosheets (S-PCN) by the pyrolysis of potassium citrate in a sealed tube at 800 °C for 2 h (Fig. 7g).[111] It was found that the interior pressure in the sealed tube caused the formation of intrinsic defects, and the density of defects could be adjusted by the volume of the sealed tube. The yield of PCNs could reach 20 wt% in the sealed tube, which was 5-fold the value in an open porcelain boat. For the samples prepared in the open porcelain boat, *in situ* generated K_2CO_3 cubes were tightly covered by smooth carbon shells. Distinct hollow carbon cubes (O-HCC) were obtained in the open porcelain boat after the removal of K_2CO_3. When prepared in the sealed tube, the rough surfaces of the carbon shells were covered by many fissures and the final S-PCNs were small-sized nanosheets. It was proposed that the pressure-induced extrusion force in the sealed tube induced the different morphologies of the two types of samples. The N_2 adsorption/desorption isotherms (Fig. 7h) confirmed the coexistence of micropores and mesopores. The SSA of S-PCN decreased from 1160 $m^2\ g^{-1}$ to 727 $m^2\ g^{-1}$ as the volume of the sealed tubes decreased from 80 mL (S-PCN-1) to 30 mL (S-PCN-3). The C_{sp} reached 277 F g^{-1} at 1 A g^{-1} for S-PCN-3 (Fig. 7i) which was about two-fold the value of O-HCC (142 F g^{-1}). S-PCN-3 exhibited a good rate performance with a C_{sp} of 144 F g^{-1} at a high current density of 200 A g^{-1}.

Zhang's group reported a highly porous and hierarchical carbon material with a high SSA of 2085 $m^2\ g^{-1}$ and V_t of 2.80 $cm^3\ g^{-1}$ synthesized from tripotassium citrate monohydrate by a ZnO template carbonization approach.[205] N_2 adsorption–desorption isotherms confirmed the coexistence of micro-/meso-/macropores in the carbon matrix. The capacitance performance was tested in 1 M H_2SO_4 with dual-redox additives of phosphotungstic acid (PTA, 15 mM) and potassium ferricyanide (KFC, 15 mM). The C_{sp} of the carbon material reached 77 F g^{-1} at 2 A g^{-1}, along with an E_{max} of 21.1 W h kg^{-1}, which were larger than the values obtained with PTA or KFC or no additive (~60 F g^{-1} for KFC, ~55 F g^{-1} for PTA, ~40 F g^{-1} for no additive).

Sevilla and coworkers evaluated the capacitance performance of highly porous N-doped carbons produced by the car-

bonization of a frozen dried mixture of potassium citrate and urea (1 : 1, w/w) in the temperature range of 700–900 °C.[113] SEM images revealed that the pyrolysis of potassium citrate/urea mixtures generated irregular particles with a conchoidal appearance. The particles were made up of an agglomeration of carbon nanoparticles (~100 nm in size) surrounded by a thin carbon layer. The pore size distribution curves confirmed the presence of numerous micropores in the range of 0.85 to 2.0 nm and small mesopores of up to 5.0 nm. It was found that the sample carbonized at 800 °C (CU-800) showed the largest SSA of 3350 $m^2 g^{-1}$ and V_t of 2.65 $cm^3 g^{-1}$. The nitrogen content decreased from 4.53 wt% for CU-700 to 0.46 wt% for CU-900. The formation of potassium cyanate and potassium cyanide during the carbonization process was evidenced from the XRD patterns. It is assumed that the developed pore structure of carbon materials derived from the mixture of urea and potassium citrate is mainly due to the interaction between the carbon matrix and potassium cyanate. The capacitance performance of CU-800 was analyzed in an ionic liquid of 1-ethyl-3-methylimidazolium bis(trifluoromethylsulfonyl)imide (EMIMTFSI) in the potential window of 0.0–3.0 V in a two-electrode cell. The CU-800-based supercapacitor delivered a C_{sp} of 44 F g^{-1} at a low rate and 25 F g^{-1} at 15 A g^{-1}. The energy density reached 56 W h kg^{-1} and retained 16 W h kg^{-1} at *ca.* 10 kW kg^{-1}.

Fan's group synthesized a N-doped aligned carbon nanosheet network (N-ACN10) from potassium citrate with MgO nanosheets as the hard template by pyrolyzing the mixture (MgO : potassium citrate = 1 : 10 w/w) under a N_2/NH_3 atmosphere at 850 °C for 1 h.[202] During the carbonization process, pyrolytic carbon moieties from potassium citrate not only deposited on the surface of MgO sheets to form carbon nanosheets but also grew on the surface of MgO templated carbon sheets to generate aligned nanosheets with sizes around 50 nm, thus resulting in a hierarchical porous structure. The HRTEM image revealed the thickness of the carbon nanosheet of N-ACN10 to be about 2 nm, and there were numerous micro-/meso-pores on the sheet due to the removal of MgO, K_2O and K_2CO_3. The SSA of N-ACN10 reached 1630 $m^2 g^{-1}$, which was 16 times the value of potassium citrate-derived CS (104 $m^2 g^{-1}$). X-ray photoemission spectroscopy (XPS) analysis confirmed that N-ACN10 contained 3.7 at% N, which was composed of pyridinic N, pyrrolic N, and graphitic N. The C_{sp} of the N-ACN10 electrode reached 331 F g^{-1} at 2 mV s^{-1}, which was more than 4 times the value of the CS electrode (76 F g^{-1}). Attributed to the interconnected nanochannels for fast ion transport, the N-ACN10 electrode exhibited superior rate capability with 203 F g^{-1} at 5 V s^{-1}. The N-ACN10 electrode also showed good cycling stability with a capacitance retention of 98% after 10 000 cycles at 200 mV s^{-1}. A high energy density of 20.6 W h kg^{-1} was obtained for a symmetrical supercapacitor tested at 0.0–1.6 V in 1 M Na_2SO_4. The energy density of the symmetrical supercapacitor reached 120.4 W h kg^{-1} when the potential window was extended to 0.0–4.0 V in 1-ethyl-3-methylimidazolium tetrafluoroborate electrolyte.

Chang *et al.* synthesized 3D coralline-like N,O-codoped microporous carbon nanosheets by the one-step pyrolysis of a mixture of potassium citrate and ammonium citrate at 800 °C for 1 h, during which the aggregation of carbon sheets was synergistically hindered by the self-activation of *in situ* generated potassium compounds (K_2CO_3 and K_2O) and the gas blowing effect of ammonium citrate.[203] By changing the mass of ammonium citrate, a series of NMCNSs were prepared and the thickness and scale of the carbon sheets decreased with an increase of ammonium citrate content. The N content increased from 1.05 at% to 3.32 at% with an increase of the ammonium citrate content, while the O content showed an inverse trend (23.43 at% to 8.86 at%). The SSA of potassium citrate-derived carbon was 943.7 $m^2 g^{-1}$, while it increased from 1659.9 $m^2 g^{-1}$ to 1900.5 $m^2 g^{-1}$ for NMCNS. The NMCNS-1 synthesized by the pyrolysis of 5 g potassium citrate and 1 g ammonium citrate showed the best capacitance performance among all the samples. The C_{sp} of NMCNS-1 reached 356 F g^{-1} at a current density of 0.5 A g^{-1} and still maintained a value of 238 F g^{-1} at 20 A g^{-1}. The NMCNS-1-based symmetric supercapacitors can withstand a high voltage of 1.8 V in 0.5 M Na_2SO_4 electrolyte. The NMCNS-1 electrode can deliver a high C_{sp} of 320.8 F g^{-1} and 136.4 F g^{-1} in KOH and Na_2SO_4 electrolytes in symmetric supercapacitors, respectively. It still maintained a value of 218 F g^{-1} at 20 A g^{-1} in KOH and retained ~52% capacitance for the Na_2SO_4-based supercapacitor.

Zhao *et al.* synthesized N,O-codoped hierarchical porous graphitic carbon by an *in situ* activation–graphitization method of directly pyrolyzing a mixture of potassium citrate, iron citrate and diammonium oxalate monohydrate (Fig. 8a).[147] The samples obtained from the direct pyrolysis of potassium citrate (PC-750) and a mixture of potassium citrate and iron citrate (PGC-750) showed a bulky monolithic morphology. With the introduction of diammonium oxalate monohydrate, a well-defined 3D honeycomb carbon framework (HPGC-750) was obtained; this was attributed to the physical activation effect of chemically released gases. The pore size distribution curves (Fig. 8b and c) confirmed that the porosity of PC-750 and PGC-750 was dominated by micropores while that of HPGC-750 was dominated by small mesopores (2–4 nm). The SSA and V_t of PC-750, PGC-750 and HPGC-750 reached 1194 $m^2 g^{-1}$, 1445 $m^2 g^{-1}$, 2973.3 $m^2 g^{-1}$ and 0.60 $cm^3 g^{-1}$, 1.25 $cm^3 g^{-1}$ and 1.62 $cm^3 g^{-1}$, respectively. XPS analysis confirmed that HPGC-750 contained 3.24 at% N and 11.65 at% O. HPGC-750 showed the best capacitance performance with a high C_{sp} of 322.6 F g^{-1} at 0.5 A g^{-1} and maintained 258.4 F g^{-1} at 30 A g^{-1} (Fig. 8d).

N,O-Co-doped hierarchically porous carbon nanosheets (NOPC) could also be synthesized by the pyrolysis of g-C_3N_4 and potassium citrate (Fig. 8e).[69] Potassium citrate could act as the carbon precursor and *endo*-templates. The pore structure and surface compositions could be regulated by g-C_3N_4. The OPC sample synthesized from potassium citrate alone exhibited an irregular nanosheet structure with a SSA of 872 $m^2 g^{-1}$ and micropore sizes centered at 0.86 nm. With the introduction of g-C_3N_4, thin and crumpled nanosheets with a high density of nanopores were formed. The pore size distri-

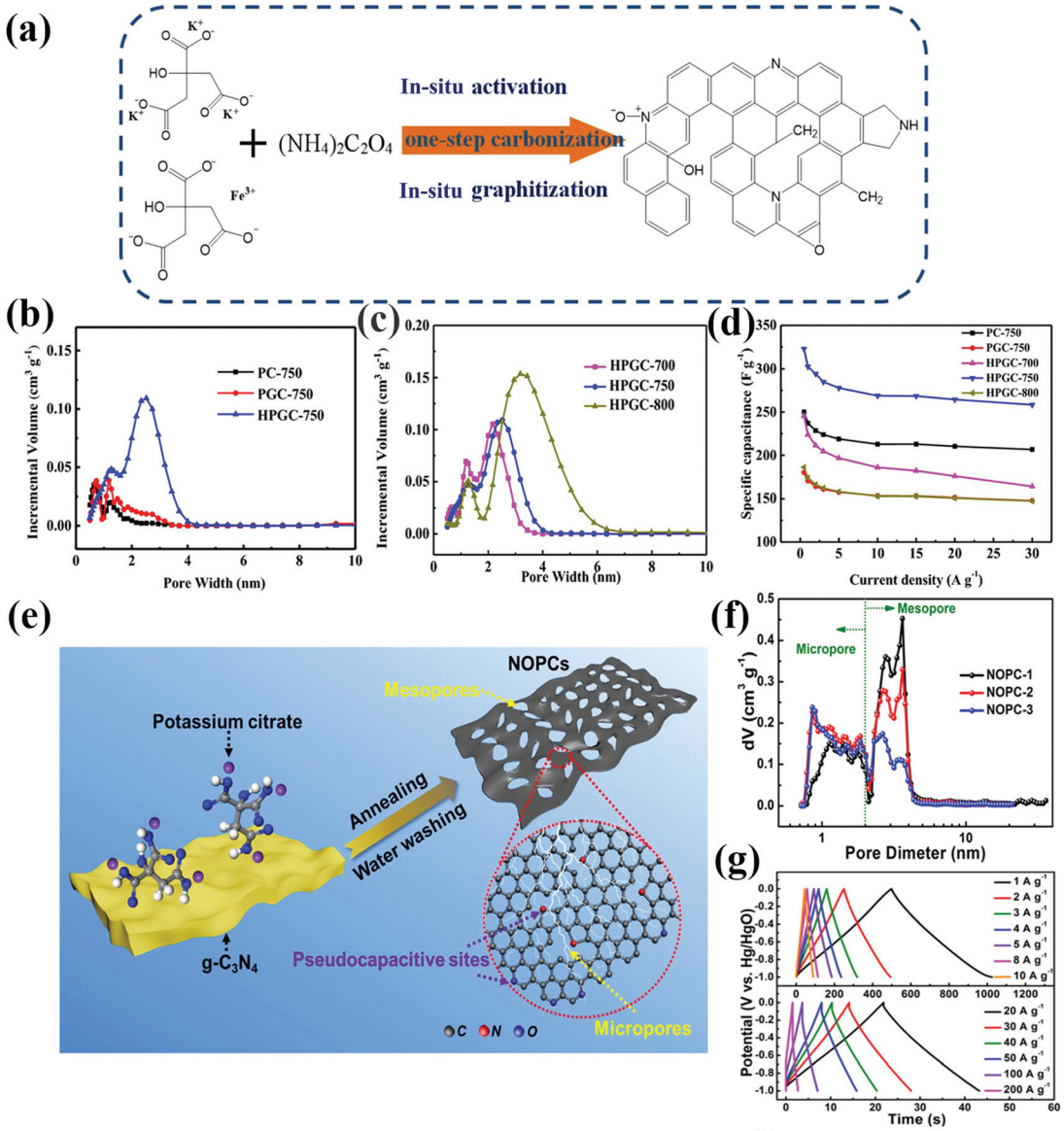

Fig. 8 (a) Schematic diagram of the synthesis of HPGC-T by direct carbonization of potassium citrate and iron citrate. (b and c) The pore size distribution curves of different samples. (d) Specific capacitance at different current densities. (e) Schematic of the synthesis process for NOPCs. (f) Pore size distribution curves of NOPCs. (g) Charge/discharge curves of NOPC-2 at various current densities. Reproduced with permission from refs. 69 and 147. Copyright 2021, Nature Publishing Group; Copyright 2021, Elsevier.

bution curves (Fig. 8f) revealed the presence of rich micropores and mesopores in NOPC. The SSA of NOPC was affected by the amount of potassium citrate. The SSA increased from 2135 $m^2\ g^{-1}$ (NOPC-1, 0.5 g g-C_3N_4 + 3 g potassium citrate) to 2557 $m^2\ g^{-1}$ (NOPC-2, 0.5 g g-C_3N_4 + 5 g potassium citrate), and then decreased to 2338 $m^2\ g^{-1}$ (NOPC-3, 0.5 g g-C_3N_4 + 7 g potassium citrate). The content of active pseudocapacitive species of pyrrolic-N/phenol-O/carboxyl-O in NOPC-2 was 9.02 at%, which was much higher than those in NOPC-1 (5.03 at%) and NOPC-3 (7.61 at%). NOPC-2 exhibited the best capacitance performance among all the samples. The charge/discharge curves (Fig. 8g) showed a slight deviation from linear shapes, indicating the presence of pseudocapacitance along with EDLC. The C_{sp} of NOPC-2 reached 527 F g^{-1} at 1 A g^{-1} and retained 339 F g^{-1} and 245.4 F g^{-1} at 100 A g^{-1} and 200 A g^{-1}, respectively. A symmetrical supercapacitor assembled based on NOPC-2 showed a C_{sp} of 104 F g^{-1} at 1 A g^{-1}, and it remained over 59% at 100 A g^{-1}. The cell also delivered good long-term cycling stability with 94.3% capacitance retention after 20 000 cycles at 10 A g^{-1}.

N,S-Co-doped three-dimensional succulent-like hierarchical carbon (NS-SHC) was synthesized by the carbonization of a supramolecular cluster made up of potassium citrate (carbon source) and thiourea (N/S source).[204] The supramolecular precursors were produced from freeze drying a solution containing thiourea (8 g) and different amounts of potassium citrate

(6 g, 8 g, 10 g). Porous carbon was obtained by pyrolyzing the supramolecular precursors at 800 °C for 2 h and acid washing. The succulent cluster structure consisted of numerous randomly directed tapered rods with diameters of about 100–200 nm. This intriguing structure for the NS-SHC series can serve as electrolyte buffering reservoirs and ensure that the active sites are well exposed to aid rapid ion/charge transport and enhance the capacitance performance. The SSA of NS-SHC increased from 192 $m^2\ g^{-1}$ to 209 $m^2\ g^{-1}$ with a decrease in the amount of potassium citrate from 10 g to 6 g. XPS analysis confirmed the presence of N (8.5 wt%) and S (2.4 wt%) in NS-SHC-8 : 8. All the NS-SHC electrodes showed enhanced capacitance performance compared to the non-doped and N-doped samples. The NS-SHC-8 : 8 electrode exhibited the best capacitance performance with a high C_{sp} of 258.5 F g^{-1} at 0.5 A g^{-1} and 206.5 F g^{-1} at 10 A g^{-1}. The NS-SHC-8 : 8 electrode also showed good cycling stability with 94.4% capacitance retention after 20 000 cycles at 100 mV s^{-1}.

Besides potassium citrate, other carbon-rich OPSs could also be used as precursors to synthesize PCNs (Table 3). Potassium humate is a popular potassium salt that is widely applied in agriculture and gardening. Potassium humate is a green precursor for producing PCNs.[206] Microporous carbon with an irregular morphology could be obtained by the direct pyrolysis of potassium humate in an inert gas.[207–209] The SSA of the resulting carbon materials spans from 589 $m^2\ g^{-1}$ to 890 $m^2\ g^{-1}$ depending on the carbonization temperature and raw reagents. The C_{sp} was above 200 F g^{-1} at a low current density (<1 A g^{-1}) in KOH electrolyte. The influence of the electrolyte on the capacitance performance was analyzed by Zhang *et al.*[208] The C_{sp} decreased in the order of acidic electrolyte (1 M H_2SO_4), basic electrolyte (3 M KOH), and neutral electrolyte (1 M Na_2SO_4). The pore structure and capacitance performance of potassium humate-derived carbon could be tuned by introducing activating agents and templates.[64,210,211] With the addition of potassium acetate as the activating agent, a large number of micropores were generated, and the SSA of the carbon materials increased from 1160 $m^2\ g^{-1}$ to 1315 $m^2\ g^{-1}$, which was more than twice that of blank sample (525 $m^2\ g^{-1}$).[210] The C_{sp} was 317 F g^{-1}, 311 F g^{-1}, and 136 F g^{-1} at 0.1 A g^{-1} in 1 M H_2SO_4, 2 M KOH, and 1 M Na_2SO_4, respectively. When using $Mn(NO_3)_2$ as a hard template, hierarchical porous carbon (NHPC) with abundant mesopores and a defective microporous morphology with structural disorder was produced (Fig. 9a) while the potassium humate-derived HPC showed a blocky structure with random meso-/macropores.[64] The adsorption–desorption isotherms of both NHPC and HPC were of combined type I/IV (Fig. 9b), revealing the hierarchical porous structure from micropores to macropores. NHPC showed a better developed mesoporous structure than the HPC, as confirmed by the more pronounced hysteresis loop. Two sharp peaks centered at ~1.9 nm and ~5.5 nm were found in the pore size distribution curves (Fig. 9c). NHPC showed a remarkably enhanced mesoporosity in the range of 5–6.5 nm in comparison with HPC. Compared to HPC, NHPC showed a slightly increased SSA, V_t, and V_m, while the total mesopore volume increased from 0.129 $cm^3\ g^{-1}$ to 0.26 $cm^3\ g^{-1}$. The charge/discharge curves of NHPC displayed typical triangular shapes at varied current densities (Fig. 9d), revealing nearly ideal EDLC behavior and good Columbic efficiency. The C_{sp} of NHPC reached 258 F g^{-1} at 0.046 A g^{-1} and retained 160 F g^{-1} at 4.65 A g^{-1} (Fig. 9e), which was much better than that of HPC (217 F g^{-1} at 0.046 A g^{-1} and 97 F g^{-1} at 3.72 A g^{-1}). The Nyquist plots (Fig. 9f) indicated that the NHPC possessed a charge transfer resistance of 2.2 Ω, which was much lower than that of HPC (7.0 Ω). NHPC showed good stability with a capacitance retention of 93.6% after 10 000 cycles at 2.32 A g^{-1}. Liu *et al.* reported a hierarchical porous carbon (HA-K-650-M-Q) prepared by the pyrolysis of a mixture of municipal sludge derived potassium humate and sodium chloride at 650 °C for 2 h, followed by calcining in air at 200 °C for 2 h and quenching in water (Fig. 9g).[70] It was found that NaCl reduced the activation energy required for carbonization, and secondary pyrolysis favored the formation of pyridinic-N and pyrrolic-N (2.06 at%). The HRTEM image showed that HA-K-650-M-Q had a pan-graphite crystal structure (Fig. 9h). Nitrogen adsorption/desorption isotherms (Fig. 9i) and pore size distribution curves (Fig. 9j) confirmed the micropore-dominated porosity of HA-K-650-M and the hierarchical pore structures of HA-K-650 and HA-K-650-M-Q. HA-K-650-M-Q showed the largest SSA of 574.4 $m^2\ g^{-1}$ with a V_t of 1.54 $m^3\ g^{-1}$. HA-K-650-M-Q also showed the best rate performance with a C_{sp} of 395 F g^{-1} at 1 A g^{-1} and retained 309 F g^{-1} at 10 A g^{-1} (Fig. 9k).

Luo *et al.* reported the synthesis of 3D sponge-like PCNs *via* the direct carbonization of potassium tartrate and sodium tartrate.[56] The pore structure of PCNs was greatly affected by the carbonization temperature. The pore structure of potassium tartrate-derived PCNs carbonized from 600 °C to 800 °C was dominated by micropores, while it contained both micropores and mesopores for the one carbonized at 900 °C. The SSA, V_t, and V_m of PCNs carbonized at 600 °C, 700 °C, 800 °C and 900 °C were 422, 847, 1017, and 1291 $m^2\ g^{-1}$, 0.20, 0.43, 0.72, and 0.49 $cm^3\ g^{-1}$, and 0.17, 0.37, 0.42, and 0.31 $cm^3\ g^{-1}$, respectively. Compared to potassium tartrate-derived PCNs, their counterpart obtained from the pyrolysis of sodium tartrate (800 °C for 1 h) showed a much lower SSA (432 $m^2\ g^{-1}$) and a smaller V_t (0.48 $cm^3\ g^{-1}$). The as-obtained PCNs could serve as conductive agent-free electrode materials for supercapacitors. The impact of the carbonization holding time (at 800 °C) on the capacitance behavior was investigated in a three-electrode system with 6 M KOH as the electrolyte. The C_{sp} decayed by ~30% for all the samples as the scan rate was raised from 5 to 200 mV s^{-1}. Besides, the sample carbonized for 1 h showed significantly lower resistance to ion motion than that of the samples carbonized for 0.5, 2, and 3 h. The 1 h sample delivered a C_{sp} of 296 F g^{-1} at 0.7 A g^{-1} and retained 213 F g^{-1} at 20 A g^{-1}. A capacitance retention of 95.1% was observed after 5000 cycles at 3 A g^{-1}. Compared to the potassium tartrate-derived PCNs, their sodium tartrate-derived counterpart showed a much worse capacitance performance. All of the sodium tartrate-derived PCNs showed a

Table 3 Pore structure and capacitance performance of other OPS derived PCNs

PCNs	OPS	Other reagents	SSA (m^2 g^{-1})	V_t (cm^3 g^{-1})	d (nm)	Electrolyte	C_{sp} (F g^{-1})	E_{max} (W h kg^{-1})	P_{max} (kW kg^{-1})	Cycle life	Rate performance	Ref.
CK800	Potassium humate	—	890	0.58	2.65	6 M KOH	232 F g^{-1} at 0.5 A g^{-1}	—	—	93.5%, 5000, at 2 A g^{-1}	114 F g^{-1} at 30 A g^{-1}	207
NHPC	Potassium humate	$Mn(NO_3)_2$	1119	0.654	—	2 M KOH	258 F g^{-1} at 0.046 A g^{-1}	—	—	93.6%, 10 000, 2.32 A g^{-1}	160 F g^{-1} at 4.65 A g^{-1}	64
CK-2	Potassium humate	Potassium acetate	1193	0.621	—	3 M KOH	311 F g^{-1} at 0.1 A g^{-1}	—	—	—	—	210
HA-K-650-M-Q	Potassium humate	NaCl	574.4	1.54	6.17	6 M KOH	395 F g^{-1} at 1 A g^{-1}	—	—	87%, 10 000, 10 A g^{-1}	309 F g^{-1} at 10 A g^{-1}	70
carbon-700	Potassium biphthalate	—	672	0.38	2.3	6 M KOH	300 F g^{-1} at 0.5 A g^{-1}	41.7	20	86.3%, 10 000, 20 A g^{-1}	43.8% at 40 A g^{-1}	212
Zn-3 : 1-900	Potassium biphthalate	Zinc metal	1605.1	1.18	3.4	6 M KOH	338.2 F g^{-1} at 1 A g^{-1}	—	—	97.8%, 10 000	100.5 F g^{-1} at 100 A g^{-1}	213
Carbon-K-800-1	Potassium tartrate	—	1018	0.49	1.93	6 M KOH	296 F g^{-1} at 0.7 A g^{-1}	—	—	95.1%, 5000, 3 A g^{-1}	213 F g^{-1} at 20 A g^{-1}	56
HSACS	Ethylenediamine tetraacetic acid di-potassium	—	2750	1.77	—	6 M KOH	268 F g^{-1} at 5 mV s^{-1}	—	—	6.7%, 10 000, 1 A g^{-1}	187 F g^{-1} at 500 mV s^{-1}	60
GK-850	Potassium gluconate	—	921.5	0.766	2.98	6 M KOH	285.8 F g^{-1} at 0.5 A g^{-1}	—	—	—	179.9 F g^{-1} at 20 A g^{-1}	214
GK-NS	Potassium gluconate	Thiourea	1026.9	0.586	2.90	6 M KOH	339.5 F g^{-1} at 0.5 A g^{-1}	—	—	97.3%, 30 000, 5 A g^{-1}	206.7 F g^{-1} at 20 A g^{-1}	214
UPCNs-700	Potassium benzoate	—	1046	0.73	2.81	6 M KOH	261 F g^{-1} at 1 A g^{-1}	—	—	—	209 F g^{-1} at 30 A g^{-1}	61
LCN-750-3	Potassium phthalimide	—	2276.7	1.108	—	6 M KOH	345 F g^{-1} at 1 A g^{-1}	16.4	20.1	94%, 10 000, 10 A g^{-1}	270 F g^{-1} at 50 A g^{-1}	65
IMPC	Poly(acrylamide-*co*-acrylic acid) potassium salt	—	1327	—	—	1 M H_2SO_4	254 F g^{-1} at 0.5 A g^{-1}	8.8	13.6	90%, 5000, 2 A g^{-1}	140 F g^{-1} at 30 A g^{-1}	53
IPC = 800	Potassium alginate	—	1145.8	0.58	2.01	6 M KOH	279 F g^{-1} at 1 A g^{-1}	—	—	96.6%, 10 000, 100 mV s^{-1}	200 F g^{-1} at 50 A g^{-1}	62

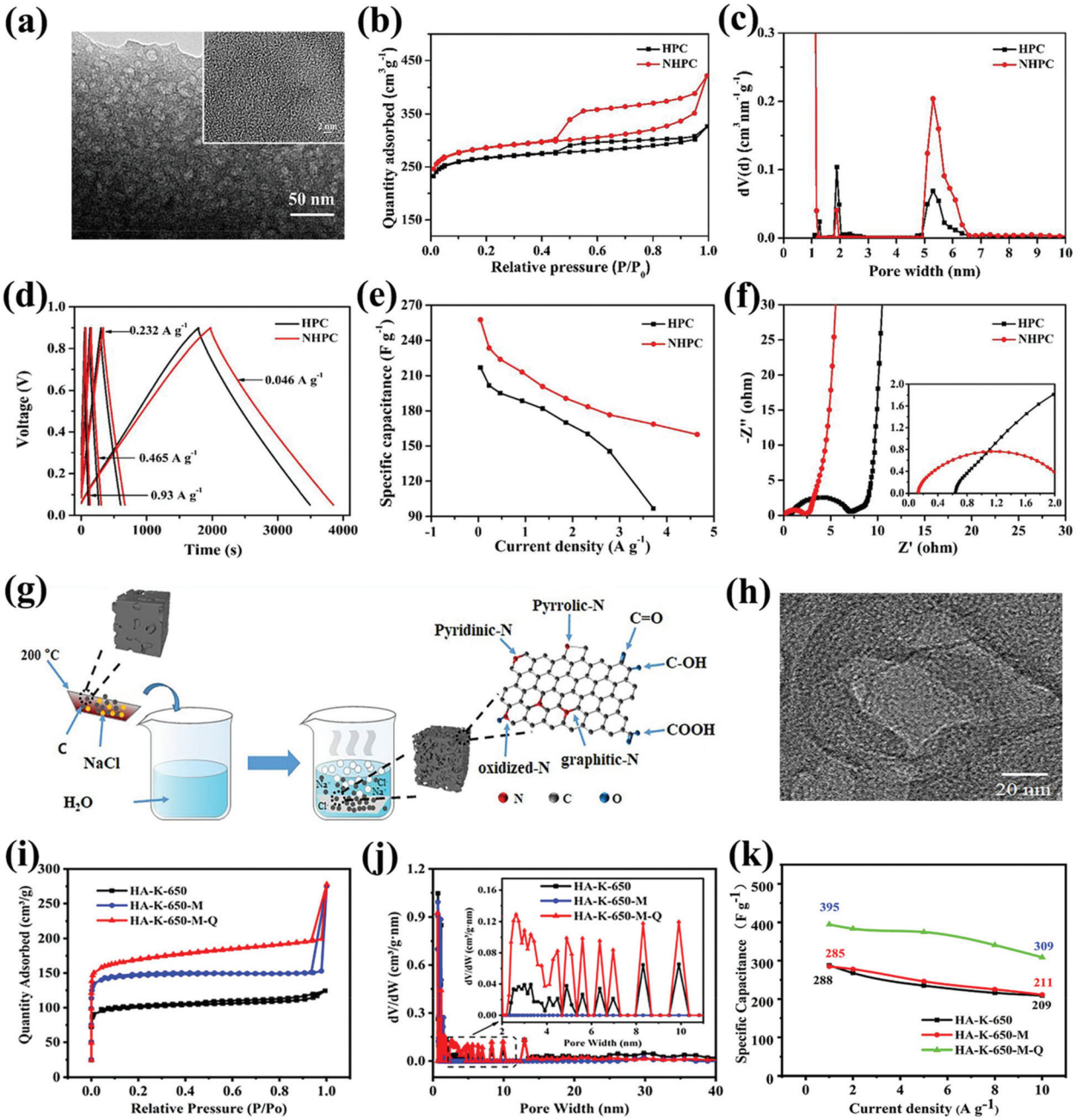

Fig. 9 (a) TEM image of NHPC demonstrating its mesoporous structure, inset shows the corresponding HRTEM image. (b) N_2 adsorption–desorption isotherms of samples. (c) Pore size distribution curves. (d) Charge/discharge curves at different current densities. (e) Specific capacitance at different current densities. (f) Nyquist plots of HPC and NHPC. (g) Schematic diagram of the synthesis of HA-K-650-Q-M. (h) HRTEM image demonstrating the porous nature of HA-K-650-Q-M. (i) N_2 adsorption–desorption isotherms of the HA-K samples and (j) corresponding pore size distribution curves. (k) Rate performance in 6 M KOH electrolyte. Reproduced with permission from refs. 64 and 70. Copyright 2019, 2021, Elsevier.

low C_{sp} below 100 F g^{-1} (at 5 mV s^{-1} and 0.9 A g^{-1}). The big capacitance difference between the potassium tartrate and sodium tartrate derived PCNs could be attributed to the large gap between the activation effect of potassium oxide and sodium oxide, which resulted in quite different porosities.

Zhang *et al.* investigated the pyrolysis behavior of seven potassium salts (*i.e.*, potassium tartrate, potassium sorbate, potassium citrate, ethylenediamine tetraacetic acid di-potassium (EDTA-2K), ethylenediamine tetraacetic acid tri-potassium, lauric acid potassium, potassium oleate) by thermogravimetric analysis, and they found that the thermal property and molecular structure of the potassium salts influenced the microstructure and porosity of the resulting PCNs.[60] The SSA values of PCNs pyrolyzed at 800 °C for 3 h were higher than 1500 m^2 g^{-1}, among which the value of EDTA-2K derived PCNs reached 3000 m^2 g^{-1}. The pore structures of PCNs from different pot-

assium salts were different, and the ratio of micropores to the total pore volume varied from 50% to 80%. The EDTA-2K derived PCNs were made up of 2D sheets with thicknesses of around 200 nm and resulted in networks on the scale of tens of micrometers. The carbon nanosheets were amorphous with distorted lattice fringes (Fig. 10a) due to incomplete graphitization. Nitrogen adsorption/desorption isotherms (Fig. 10b) and pore size distribution curves (Fig. 10c) confirmed that the porosity of EDTA-2K derived carbons (pyrolyzed at 850 °C for 3 h) was rich in micropores (0.5 nm to 2 nm) and mesopores (2 nm to 4 nm). The SSAs of EDTA-2K derived PCNs pyrolyzed from 700 to 900 °C for 3 h were all larger than 2500 $m^2 g^{-1}$. The SSA increased from 2676 $m^2 g^{-1}$ to 3179 $m^2 g^{-1}$ and the V_t increased from 1.4 $cm^3 g^{-1}$ to 3.4 $cm^3 g^{-1}$ from 700 to 850 °C, while the SSA further decreased above 850 °C due to the merging of micropores into mesopores. The V_m of PCNs increased slowly when the pyrolysis temperature was raised from 700 to 850 °C and then decreased at temperatures above 850 °C, resulting in the changes of the SSA. However, the V_t was almost enhanced by 100% as the temperature was raised from 800 to 850 °C; this was attributed to the merging of micropores into mesopores. The V_t and V_m of PCNs both decreased at 900 °C due to the formation of macropores. The rectangular shape of the CV curves at different scan rates (Fig. 10d) and the triangular shape of the charge–discharge curves recorded at different current densities (Fig. 10e) confirmed the EDLC behavior of HSACS (EDTA-2K pyrolyzed at 750 °C). HSACS displayed the best capacitance performance among all the samples carbonized at different temperatures with the largest C_{sp} of 268 F g^{-1} at 5 mV s^{-1} and a good rate performance (187 F g^{-1} at 500 mV s^{-1}). The HSACS electrode showed a comparable capacitance performance in 1 M H_2SO_4 with 270 F g^{-1} at 0.5 A g^{-1} and 195 F g^{-1} at 20 A g^{-1}. Furthermore, the HSACS electrode retained a high C_{sp} of 266 F g^{-1} at 0.5 A g^{-1} and 200 F g^{-1} at 10 A g^{-1} within a 1.6 V potential window in 2 M Li_2SO_4 electrolyte (Fig. 10f). The symmetrical supercapacitor showed an E_{max} of 23.6 W h kg^{-1} and a P_{max} of 6.4 kW kg^{-1}.

Kang and coauthors reported the synthesis of a highly porous carbon *via* simple thermal treatment of potassium acetate and investigated the effect of pyrolysis temperature and holding time on the porosity, electrical conductivity, and capacitance performance of the resulting PCNs.[215] SEM images revealed that the products were clusters of irregular-sized carbon flakes. The porosity analysis results indicate that the SSA, V_t, and V_m increased from 811 $m^2 g^{-1}$ to 1325 $m^2 g^{-1}$, from 0.368 $cm^3 g^{-1}$ to 0.594 $cm^3 g^{-1}$, and from 0.280 $cm^3 g^{-1}$ to 0.486 $cm^3 g^{-1}$, respectively, with increasing pyrolysis temperature from 700 °C to 900 °C and a fixed holding time of 1 h. When fixing the pyrolysis temperature at 900 °C, the SSA, V_t, and V_m increased from 1266 $m^2 g^{-1}$ to 1704 $m^2 g^{-1}$, from 0.562 $cm^3 g^{-1}$ to 0.887 $cm^3 g^{-1}$, and from 0.476 $cm^3 g^{-1}$ to 0.742 $cm^3 g^{-1}$, respectively, upon extending the holding time to 4 h, but decreased to 1183 $m^2 g^{-1}$, 0.750 $cm^3 g^{-1}$, and 0.484 $cm^3 g^{-1}$, respectively, when the holding time was further extended to 10 h. The electrical conductivity increased from 4089 S cm^{-1} to 22 950 S cm^{-1} upon extending the holding time to 10 h. The capacitance performance of PCNs was tested in coin-type supercapacitors in 6 M KOH electrolyte. It was found out that the C_{sp} did not increase linearly with the SSA and electrical conductivity of PCNs. The sample synthesized by pyrolysis at 900 °C for 1 h showed the largest C_{sp} of 195 F g^{-1} at 0.5 A g^{-1} among all the samples. The rate capability at high

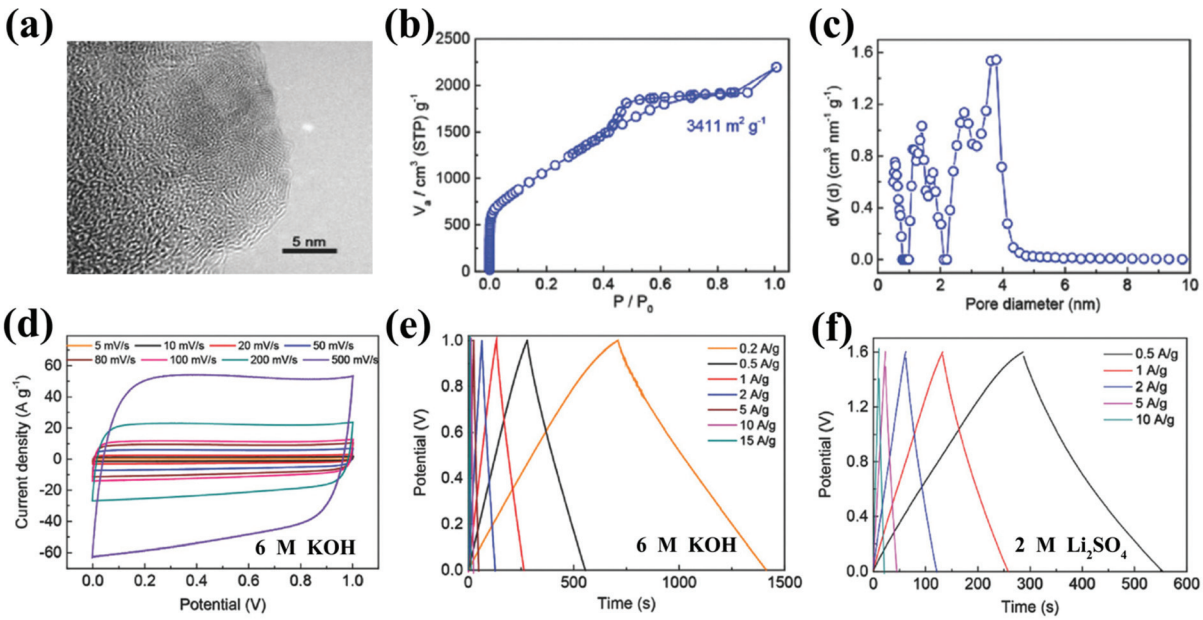

Fig. 10 (a) HRTEM image of EDTA-2K derived carbon. (b) N_2 adsorption–desorption isotherms and (c) pore size distribution curve of HSACS pyrolyzed at 850 °C for 3 h. (d) CV curves of HSACS at different scan rates. Charge/discharge curves of the HSACS at different current densities in (e) 6 M KOH electrolyte and (f) 2 M Li_2SO_4 aqueous electrolyte. Reproduced with permission from ref. 60. Copyright 2018, Wiley.

scan rates and large current densities was enhanced from 43% to 91% by increasing the holding time to 4 h; this was attributed to the widened pore size at a longer holding time. The supercapacitor also showed excellent cycling stability with a capacitance retention of 99.0% after 80 000 cycles at 5 A g^{-1}.

Fuertes and coauthors reported the synthesis of N-doped microporous carbons by the pyrolysis of a mixture of melamine and potassium gluconate.[52] It was found that the pyrolysis temperature had a great influence on the porosity of carbonaceous products. The samples carbonized at 500 °C and 650 °C were almost non-porous (SSA < 5 m^2 g^{-1}). The samples carbonized at 800 °C to 900 °C possessed SSAs of 660–1040 m^2 g^{-1} and V_t of 0.29–0.42 cm^3 g^{-1}. It was also found that the SSA and V_m increased with a decrease of the amount of melamine in the recipe. SEM images revealed that the N-doped samples synthesized at ≥800 °C possessed a sponge-like structure made up of fully interconnected thin layers. In comparison with the N-doped samples, the undoped samples showed better textural development. The undoped sample synthesized from the pyrolysis of potassium gluconate at 800 °C for 1 h (C-KG) possessed tremendous micropores and mesopores with a SSA of 1410 m^2 g^{-1} and a V_t of 0.76 cm^3 g^{-1}. The elemental analysis results indicated that the N wt% and the N/C atomic ratio increased with an increase of the melamine content but decreased with an increase of the pyrolysis temperature. The conductivity decreased with an increase in the N content. The electrical conductivity of C-KG was 3.7 S cm^{-1}, which was much higher than that of its N-doped counterpart synthesized at ≥800 °C (2.5, 0.4 and 0.03 S cm^{-1} for CN-900-2, CN-850-2 and CN-800-2, respectively). The capacitance performance of the porous carbon was tested in 1 M H_2SO_4 electrolyte in a two-electrode system. The results indicated that, compared to the C_{sp} values (170–186 F g^{-1}) of the doped samples, the undoped sample showed a slightly enhanced C_{sp} (190 F g^{-1} at 0.1 A g^{-1}) and better rate performance. CN-850-2 exhibited a better capacitance performance than those of CN-900-2 and CN-800-2 with an E_{max} of 10.2 W h kg^{-1} and a P_{max} of 5.7 kW kg^{-1} at 1.2 V. The symmetrical supercapacitor also exhibited good stability with the C_{sp} decreasing by only 2% after 6000 cycles at 5 A g^{-1}.

Li and coworkers reported the synthesis of N/S co-doped ultrathin carbon nanosheets (GK-NS) by carbonizing a mixture of potassium gluconate and thiourea (8 : 1, w/w) at 850 °C for 1 h (Fig. 11a).[214] GK-NS exhibited a very thin thickness ranging from ~108 nm to ~720 nm and possessed an amorphous structure (Fig. 11b). The relative atomic percentages of N and S in GK-NS reached 12.74 at% and 2.88 at%, respectively. Nitrogen adsorption/desorption isotherms (Fig. 11c) and pore size distribution curves (Fig. 11d) confirmed the microporous structure of GK-NS and hierarchical pore structures of the other samples. The SSA and V_t of GK-NS were 1026.96 m^2 g^{-1} and 0.568 cm^3 g^{-1}, respectively, which were comparable to those of their undoped counterparts (921.51 m^2 g^{-1} and 0.766 cm^3 g^{-1}). The undoped samples were synthesized by the pyrolysis of potassium gluconate from 750 °C to 900 °C for 1 h. The SSA increased with an increase in the temperature and reached a maximum at 850 °C. The C_{sp} of GK-NS reached 339.5 F g^{-1} at 0.5 A g^{-1} and retained 206.7 F g^{-1} at 20 A g^{-1} (Fig. 11e), which was much larger than that of the undoped samples (200.0 to 285.8 F g^{-1} at 0.5 A g^{-1} and 88.0 to 179.9 F g^{-1} at 20 A g^{-1}). For a symmetrical supercapacitor assembled from GK-NS and 6 M KOH electrolyte, the E_{max} and P_{max} reached 11.2 W h kg^{-1} and 10.0 kW kg^{-1}, respectively. The potential window of the symmetrical supercapacitor could be extended to 2.0 V, resulting in an even higher energy density of 24.5 W h kg^{-1} and a power density of 20.0 kW kg^{-1}.

Wu *et al.* also explored the capacitance performance of a N/S co-doped porous carbon (NSHPC) derived from potassium gluconate and thiourea by two-step pyrolysis.[183] The undoped samples were synthesized by pyrolyzing potassium gluconate from 600 °C to 800 °C for 2 h. The sample obtained at 700 °C (HPC-700) was mixed with thiourea (1 : 3, w/w) and further heat treated at 750 °C for 2 h to produce NSHPC (Fig. 11f). The TEM image revealed that the three-dimensional interconnected porous framework of NSHPC was formed by a substantial amount of highly interconnected mesopores (Fig. 11g). Nitrogen adsorption/desorption isotherms (Fig. 11h) and pore size distribution curves (Fig. 11i) further confirmed the mesoporous structure of the HPC samples. The SSA increased from 370 m^2 g^{-1} to 920 m^2 g^{-1}, and V_t increased from 0.36 cm^3 g^{-1} to 0.69 cm^3 g^{-1} with an increase of the pyrolysis temperature. After doping treatment, the SSA and V_t increased slightly (721 m^2 g^{-1} and 0.69 cm^3 g^{-1}, respectively). The relative atomic percentages of N and S in NSHPC were 4.3 at% and 1.2 at%, respectively. The CV curve of NSHPC displayed a relatively rectangular shape in contrast with the other samples, indicating better capacitive characteristics of NSHPC (Fig. 11j). The higher current response of NSHPC indicated it had a larger specific capacitance than the other samples. The deviation of the CV curve from an ideal rectangular shape and slightly distorted triangular contour of the charge/discharge curves (Fig. 11k) indicated the presence of pseudocapacitance. The C_{sp} of NSHPC reached 320 F g^{-1} at 0.5 A g^{-1} and retained 200 F g^{-1} at 50 A g^{-1} (Fig. 11l) which was a little larger than that of HPC-700 (~285 F g^{-1} at 0.5 A g^{-1} and ~170 F g^{-1} at 50 A g^{-1}).

Li *et al.* reported a facile approach to prepare ultrathin porous carbon nanosheets (UPCNs) by the carbonization of potassium benzoate from 600 °C to 800 °C for 2 h.[61] The UPCNs were assembled from crumpled sheets with sizes from hundreds of nanometers to several micrometers. The thickness of the sample pyrolyzed at 700 °C (UPCNs-700) was approximately 1.7 nm. The porosity analysis results indicated that the SSA, V_t, and V_m increased from 597.8 m^2 g^{-1} to 1542.2 m^2 g^{-1}, from 0.53 cm^3 g^{-1} to 1.02 cm^3 g^{-1}, and from 0.22 cm^3 g^{-1} to 0.62 cm^3 g^{-1}, respectively, with increasing pyrolysis temperature from 600 °C to 800 °C. The average pore diameter decreased from 3.52 nm to 2.63 nm with an increase of pyrolysis temperature. It was found that UPCNs-700 displayed the best capacitance performance. The C_{sp} of UPCNs-700 reached 261 F g^{-1} at 1 A g^{-1} and retained 209 F g^{-1} at 30 A g^{-1}. The C_{sp} of the UPCNs-600 and UPCNs-800 were 189 F g^{-1} and 165.8 F g^{-1} at 1 A g^{-1}, respectively. A symmetrical supercapacitor based on UPCNs-700 presented an E_{max} and P_{max} of

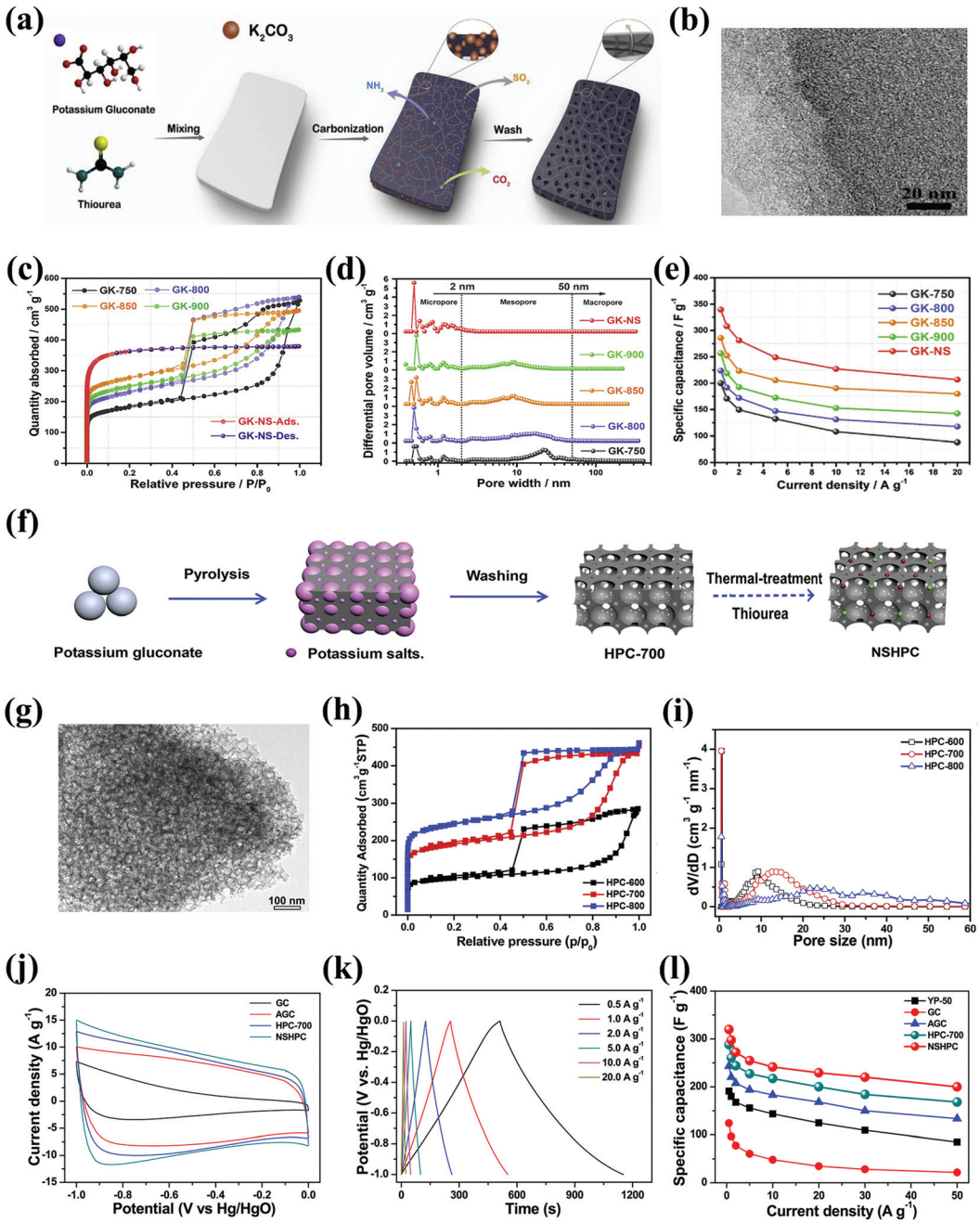

Fig. 11 (a) Schematic of the preparation procedure of N/S co-doped carbon nanosheets. (b) TEM image of GK-NS. (c) N_2 adsorption/desorption isotherms, (d) pore size distribution curves and (e) rate performance of GK-X. (f) Schematic diagram illustrating the synthesis process for NSHPC. (g) TEM image of NSHPC. (h) N_2 adsorption/desorption isotherms, (i) pore size distribution curves of the HPC-X samples. (j) CV curves of the porous carbon electrodes at 50 mV s^{-1}. (k) GCD curves of the NSHPC electrode at different current densities. (l) Specific capacitance at various current densities. Reproduced with permission from refs. 214 and 183. Copyright 2019, Elsevier.

11.73 W h kg^{-1} and 12.3 kW kg^{-1}, respectively. The symmetrical supercapacitor also exhibited good stability with C_{sp} decreasing by 5% after 5000 cycles at 20 A g^{-1}.

Puthusseri and coauthors reported beehive-like PCNs assembled from interconnected microporous carbon (IMPC) sheets by the direct pyrolysis of poly(acrylamide-*co*-acrylic acid) potassium salt at 1000 °C without adding any activation agents or additional templates.[53] K_2CO_3 was formed *in situ* during carbonization and generated pores by reacting with the carbon framework, resulting in a high SSA of 1327 m^2 g^{-1}. The pore structure of IMPC was dominated by micropores with pore sizes ranging from 1 to 2 nm, which contributed to 80% of V_t. 1.9% of nitrogen and 10% of oxygen were detected by XPS. The capacitance performance of IMPC was tested in both aqueous (1 M H_2SO_4) and non-aqueous (1 M $LiPF_6$ in ethylene carbonate–dimethyl carbonate) electrolytes in a two-electrode system. The C_{sp} reached 254 F g^{-1} at 0.5 A g^{-1}

and maintained 150 F g^{-1} at 30 A g^{-1} in 1 M H_2SO_4. The maximum power density was 13.6 kW kg^{-1} with an energy density of 3.1 W h kg^{-1}. A capacitance retention of 90% was observed after 5000 cycles at 2 A g^{-1}. The C_{sp} was 138 F g^{-1} at 0.25 A g^{-1} and retained 100 F g^{-1} at 10 A g^{-1} with an E_{max} of 31 W h kg^{-1} and a maximum P_{max} of 11 kW kg^{-1} in non-aqueous electrolyte.

As a carbon-rich natural polymer, potassium alginate can also function as a carbon precursor to prepare PCNs. Sun *et al.* reported a facile and scalable way to prepare three-dimensional interconnected porous carbons by the pyrolysis of potassium alginate.[62] With an increase of the pyrolysis temperature (from 700 °C to 900 °C), the carbon wall gradually fragmented, and the pore size was enlarged due to the merging of micropores into mesopores. The porosity analysis results indicated that the SSA and V_t increased from 722.0 m^2 g^{-1} to 1281.8 m^2 g^{-1}, and from 0.35 cm^3 g^{-1} to 0.72 cm^3 g^{-1}, respectively, with increasing pyrolysis temperature from 700 °C to 900 °C. The sample produced by pyrolysis at 800 °C (IPC-800) showed an intermediate SSA of 1145.8 m^2 g^{-1} with a V_t of 0.58 cm^3 g^{-1}. IPC-800 displayed the best capacitance performance among the three samples. The C_{sp} of IPC-800 reached 279 F g^{-1} at 1 A g^{-1} and retained 200 F g^{-1} at 50 A g^{-1}. The IPC-800 electrode also exhibited good stability with 96.6% capacitance retention after 10 000 cycles at 100 mV s^{-1}. It also revealed that the potential window could be extended to 1.6 V in 1 M Na_2SO_4, contributing to a high energy density of 16.9 W h kg^{-1}.

Carbon-rich OPSs are promising precursors for producing PCNs. Among various OPSs, potassium citrate is the most frequently used one for the synthesis of PCNs; this is attributed to its low price and relatively high yield of PCNs.[60] Taking sustainability into consideration, renewable source derived OPSs including potassium citrate/gluconate/tartrate/humate/alginate, *etc.* are preferred for the design and synthesis of PCNs. Porous carbon nanosheets and assembled sponge structures could be obtained by the direct pyrolysis of OPSs with relatively high oxygen content (*e.g.*, potassium citrate/tartrate/gluconate/benzoate, and ethylenediamine tetraacetic acid di-potassium), owing to the prominent chemical blowing/foaming effect of H_2O, CO_2 and other volatile substances. Blocky structures of PCNs with irregular shapes will be formed by the pyrolysis of OPSs with relatively low oxygen content (*e.g.*, potassium humate/biphthalate/alginate) due to fusion, condensation of the precursor and an inconspicuous foaming effect. Carbon nanosheets also could be prepared from OPSs with a relatively low oxygen content by introducing templates. Porous carbon nanosheets always show a greatly enhanced capacitance performance compared to that of their counterparts with blocky structures.

6. Capacitance performance of PCNs synthesized with OPSs as activation agents and partial carbon sources

As discussed above, OPSs can serve as both carbon sources and activation agents in the preparation of PCNs. However, the option of using OPSs is limited when taking cost, yield of PCNs, pore structure and other factors into consideration. It is meaningful to combine them with other carbon sources, especially renewable sources, to extend the multifunctional effects of OPSs (Table 4).

Among various OPSs, potassium citrate is often chosen to be combined with other precursors such as resorcinol/formaldehyde resin, petroleum asphalt, carbon black, cellulose, and agar to prepare PCNs for supercapacitors.[57,216–220] Carbon nanofiber (CNF)-bridged porous carbon nanosheets (PCNs) could be obtained by the pyrolysis of a mixture of bacterial cellulose and potassium citrate at 850 °C (Fig. 12a).[57] Potassium citrate not only served as the carbon source for the formation of PCNs, but also generated potassium as a chemical activation agent during the pyrolysis process. In the CNF-bridged PCNs, the small size of the CNFs could provide a large specific surface area for charge accommodation and also function as a spacer to inhibit the aggregation of PCNs. Meanwhile, the 3D interconnected network structure was vital for the rapid diffusion/transport of electrons and electrolyte ions in all directions. N_2 adsorption/desorption isotherms (Fig. 12b) displayed combined characteristics of type I and IV isotherms, revealing the presence of micropores and mesopores. The pore size distribution curves (Fig. 12c) further confirmed the existence of micropores and mesopores. The SSA and V_t of the PCN/CNF composite reached 1037 m^2 g^{-1} and 1.04 cm^3 g^{-1}; these values were much larger than those of CNFs (510 m^2 g^{-1} and 0.74 cm^3 g^{-1}) and PCNs (381 m^2 g^{-1} and 0.37 cm^3 g^{-1}). The charge/discharge curves of PCN/CNF exhibited little deviation from the typical isosceles triangular shape (Fig. 12d), indicating the presence of pseudocapacitance owing to the oxygen-containing functional groups. The C_{sp} of PCN/CNF was 261 F g^{-1} at 2 mV s^{-1} and retained 200 F g^{-1} with a retention ratio of 76.6% at 500 mV s^{-1} (Fig. 12e). The symmetric supercapacitor could deliver an E_{max} of 20.4 W h kg^{-1} and a P_{max} of 17.8 kW kg^{-1}.

A series of porous carbon nanosheet-assembled hierarchical architectures (NHCAs) were synthesized by using potassium citrate as the activation agent as well as an *in situ* template and petroleum asphalt as the precursor (Fig. 12f).[220] Direct pyrolysis of petroleum asphalt only produced irregular carbon particles. By introducing potassium citrate, pores with sizes of microns could be generated and the thickness of the pore-walls could be further decreased by increasing the dosage of potassium citrate (Fig. 12g). N_2 adsorption/desorption isotherms of NHCAs displayed type I characteristics, demonstrating the presence of rich micropores (Fig. 12h). The small hysteresis loop at medium pressure disclosed the existence of a low content of mesopores. The pore size distribution curves (Fig. 12i) further confirmed the microporous structure of NHCAs. The SSA and V_t of NHCAs increased from 836 m^2 g^{-1} and 0.41 cm^3 g^{-1} to 1437 m^2 g^{-1} and 0.60 cm^3 g^{-1} upon increasing the mass ratio of petroleum asphalt to potassium citrate from 1 : 2 to 1 : 6. NHCA-4 obtained from a mass ratio of 1 : 4 exhibited the best capacitance performance. The C_{sp} of NHCA-4 reached 307 F g^{-1} at 0.05 A g^{-1} (Fig. 12j) which was

Table 4 Pore structure and capacitance performance of PCNs prepared from renewable sources

PCNs	OPS	Other reagents	SSA (m^2 g^{-1})	V_t (cm^3 g^{-1})	Electrolyte	C_{sp} (F g^{-1})	E_{max} (W h kg^{-1})	P_{max} (kW kg^{-1})	Cycle life	Rate performance	Ref.
PCN/CNF	Potassium citrate	Bacterial cellulose	1037	1.04	6 M KOH	261 F g^{-1} at 2 mV s^{-1}	—	—	97.6%, 10 000, 200 mV s^{-1}	200 F g^{-1} at 500 mV s^{-1}	57
HCF-0.5	Potassium citrate	Resorcinol/formaldehyde resin	1359	0.85	6 M KOH	224 F g^{-1} at 1 A g^{-1}	—	—	~93.3%, 1000, 1 A g^{-1}	191 F g^{-1} at 10 A g^{-1}	216
100MHPC-3	Potassium citrate	Super P powder	1280.4	0.6657	6 M KOH	318 F g^{-1} at 1 A g^{-1}	—	—	88%, 10 000, 5 A g^{-1}	212 F g^{-1} at 100 A g^{-1}	218
S-850	Potassium citrate	Poplar catkin	2186	1.35	6 M KOH	280 F g^{-1} at 1 A g^{-1}	—	—	—	170 F g^{-1} at 20 A g^{-1}	222
NHCA-4	Potassium citrate	Petroleum asphalt	1267	—	6 M KOH	307 F g^{-1} at 0.05 A g^{-1}	10.7	5.9	93.4%, 10 000, 5 A g^{-1}	~215 F g^{-1} at 20 A g^{-1}	220
PC	Potassium citrate	Agar	1070	—	6 M KOH	309 F g^{-1} at 1 A g^{-1}	—	—	—	225 F g^{-1} at 50 A g^{-1}	217
NPC		Agar, urea	1300	—		357 F g^{-1} at 1 A g^{-1}			95.5%, 10 000, 200 mV s^{-1}	267 F g^{-1} at 50 A g^{-1}	217
NPC-700-2-2	Potassium citrate	Polyacrylamide	1147.3	0.562	6 M KOH	351 F g^{-1} at 1 A g^{-1}	—	—	98.4%, 10 000, 200 mV s^{-1}	226 F g^{-1} at 50 A g^{-1}	221
HPCFs-2.5	Potassium citrate	Resorcinol/formaldehyde resin	—	—	6 M KOH	196 F g^{-1} at 1 A g^{-1}	—	—	—	—	219
N-HPCFs-2.5	Potassium citrate	Melamine, resorcinol/formaldehyde resin	1759	0.83	6 M KOH	298 F g^{-1} at 1 A g^{-1}	—	—	~90%, 5000, at 1 A g^{-1}	263 F g^{-1} at 10 A g^{-1}	219
D-SCN	Potassium benzoate	Coal tar pitch, *N,N′*-diphenylthiourea	2285	1.11	2 M KCl	458 F g^{-1} at 0.1 A g^{-1}	—	—	—	282 F g^{-1} at 50 A g^{-1}	68

twice the value of potassium citrate derived HCA (152 F g^{-1}). NHCA-4 showed a good rate performance with a C_{sp} of 224 F g^{-1} at 20 A g^{-1} (73%), and good stability with a capacitance retention of 93.4% after 10 000 cycles at 5 A g^{-1}.

Wang *et al.* synthesized a N,O-codoped porous carbon with an interconnected structure (NPC) by the one-step pyrolysis of a mixture of polyacrylamide and potassium citrate at 600 °C to 800 °C.[221] It was revealed that the SSA of the PCNs increased with an increased carbonization temperature and extended holding time. The NPC-700-2-2 sample pyrolyzed at 700 °C for 2 h with a mass ratio of 1 : 2 (polyacrylamide to potassium citrate) displayed a moderate SSA of 1147.3 m^2 g^{-1} and V_t of 0.562 cm^3 g^{-1}, but exhibited the best capacitance performance among all the samples. SEM images demonstrated a 3D interconnected porous structure with massive pores on the scale of microns and the HRTEM image revealed the microporous features of the carbon wall (Fig. 12k) with sizes centered at 0.63 and 1.20 nm. By contrast, other samples showed a wider pore size distribution with a small number of mesopores distributed at 2–4 nm (Fig. 12l). The C_{sp} of NPC-700-2-2 reached 351 F g^{-1} at 1 A g^{-1} (Fig. 12m), which was much higher than those of polyacrylamide derived carbon (91 F g^{-1}), potassium citrate derived carbon (186 F g^{-1}), and other NPCs. The sample also showed a good rate performance with a C_{sp} of 226 F g^{-1} at 50 A g^{-1} (64%) and a good stability with a capacitance retention of 98.4% after 10 000 cycles at 200 mV s^{-1} in 6 M KOH electrolyte. The symmetric supercapacitor based on NPC-700-2-2 could be operated over a wide potential window of 0 to 1.6 V and displayed an E_{max} of 21.4 W h kg^{-1} in 1 M Na_2SO_4 electrolyte.

Recently, Luo *et al.* proposed a one-step approach to prepare hierarchically porous carbon by pyrolysis of potassium-citrate-loaded poplar catkin at 750 °C to 900 °C.[222] All the samples showed massive pores with sizes of about 1–2 μm constructed from interconnected carbon walls. The SSA increased from 1337.8 m^2 g^{-1} for S-750 to 2185.6 m^2 g^{-1} for S-850 and decreased to 1894.3 m^2 g^{-1} for S-900. The V_t showed the same tendency as that of SSA and increased from 0.63 cm^3 g^{-1} for S-750 to 1.35 cm^3 g^{-1} for S-850 and decreased to 1.15 cm^3 g^{-1} for S-900. The S-850 sample displayed a superior specific capacitance with little significant chemical blowing/foaming effect of potassium citrate. Both the renewable sources (*e.g.*, bacterial cellulose, agar, poplar catkin) and the chemical reagents (*e.g.*, resin, polyacrylamide, petroleum asphalt) could serve as the carbon source to produce PCNs with the aid of potassium citrate.[57,217,219–222] The SSA and V_t could be facilely adjusted by varying the pyrolysis temperature and the mass ratio of carbon source to potassium citrate. The porosity of PCNs was dominated by micropores. With rising pyrolysis temperature and an increase of the mass ratio of potassium citrate, the specific capacitance reached 281 F g^{-1} at 1 A g^{-1}, while S-900 showed a higher specific capacitance under a high current density (190 F g^{-1} at 20 A g^{-1}). The symmetric supercapacitor based on S-850 could be operated over a potential window of 0 to 1.4 V and displayed an E_{max} of 13.3 W h kg^{-1} and a P_{max} of 14.0 kW kg^{-1} in 1 M Na_2SO_4 electrolyte.

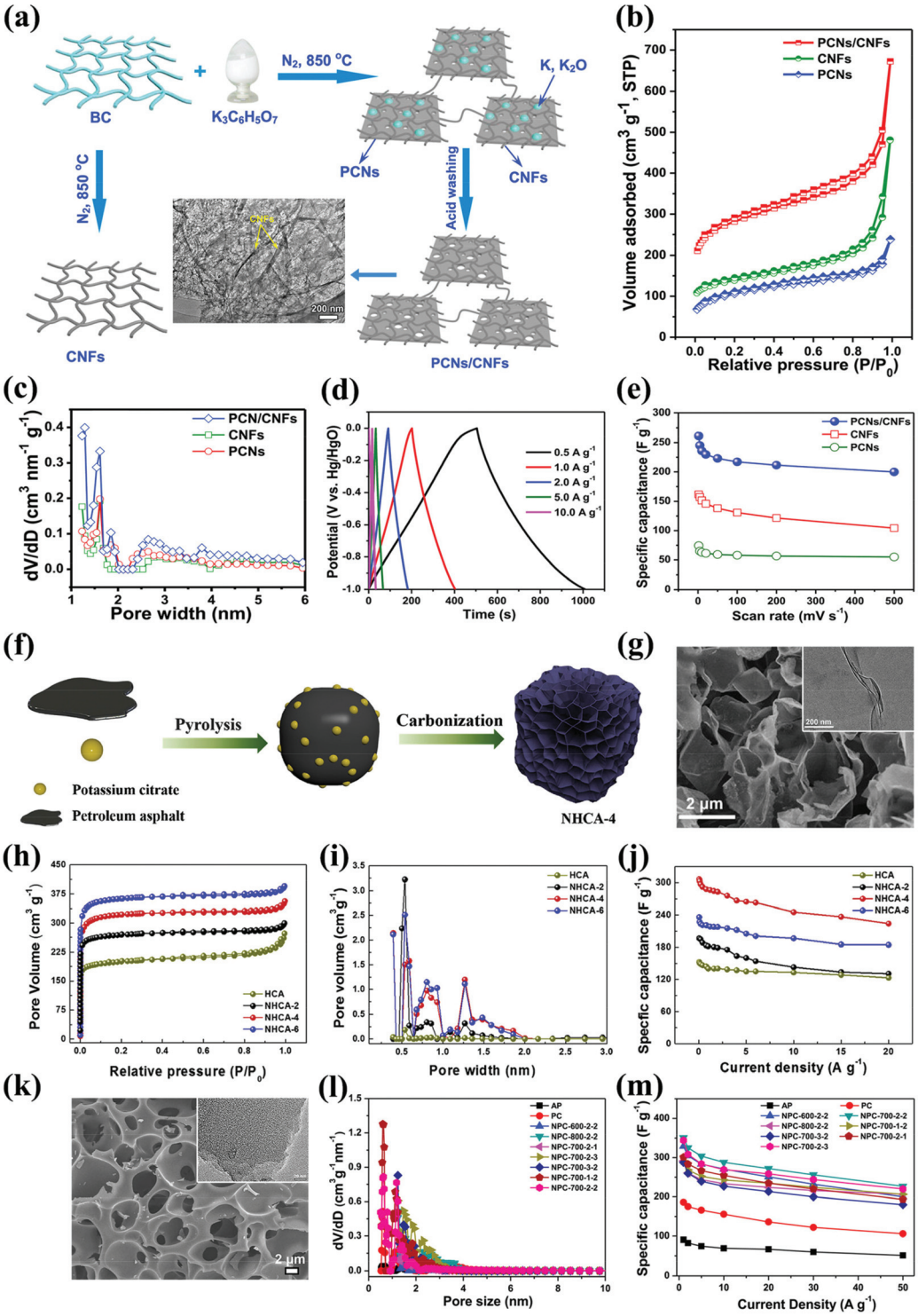

Fig. 12 (a) Schematic of the synthesis process for the PCN/CNF composite; inset shows the TEM image of the PCN/CNF composite. (b) N_2 adsorption/desorption isotherms and (c) pore size distribution curves of porous carbon materials. (d) charge/discharge curves of the PCN/CNF composite at varied current densities. (e) Specific capacitance at different scan rates. (f) Schematic diagram of the synthesis of NHCA-4. (g) SEM image of the NHCA-4; inset shows the corresponding TEM image. (h) N_2 adsorption/desorption isotherms and (i) pore size distribution curves of HCA and NHCAs. (j) The rate performance of HCA and NHCAs. (k) SEM image of NPC-700-2-2; inset shows the corresponding TEM image. (l) Pore size distribution curves of samples. (m) Specific capacitance at different current densities. Reproduced with permission from refs. 57, 220 and 221. Copyright 2016, 2019, 2019, Elsevier.

Highly porous carbon materials could be synthesized by introducing potassium citrate into the recipe as the carbon source, such that the contribution of mesopores to SSA and V_t would be enhanced. The SSA and V_t reached 2185.6 m^2 g^{-1} and 1.35 cm^3 g^{-1} for the optimal sample.[222] Blocky carbon materials with a SSA less than 100 m^2 g^{-1} were obtained without potassium citrate.[217,221,222] Compared to the C_{sp} of control samples (91 F g^{-1} to 161 F g^{-1}) prepared without potassium citrate, the C_{sp} of those samples synthesized with the addition of potassium citrate showed a greatly enhanced capacitance performance (261 F g^{-1} to 357 F g^{-1}).[57,217,219–222]

Besides potassium citrate, potassium benzoate is also used in combination with other precursors to produce functional PCNs. Zhang *et al.* synthesized N/S dual-doped stacked carbon nanosheets (D-SCN) from coal tar pitch in the presence of potassium benzoate and *N*,*N*′-diphenylthiourea (Fig. 13a).[68] A plausible mechanism for the formation of nanosheets is depicted in Fig. 13b. The partial decomposition of MCTP at 200–500 °C generated considerable micropores, providing massive conduits for the impregnation of potassium benzoate. Potassium benzoate melted and reacted with the carbon to yield appreciable K_2O and K_2CO_3 at temperatures up to ~500 °C, which were decomposed further to generate potassium. Due to strong permeability, potassium could intercalate into the carbon matrix to produce the KC_x compounds. The KC_x compounds then decomposed, and the regenerated pot-

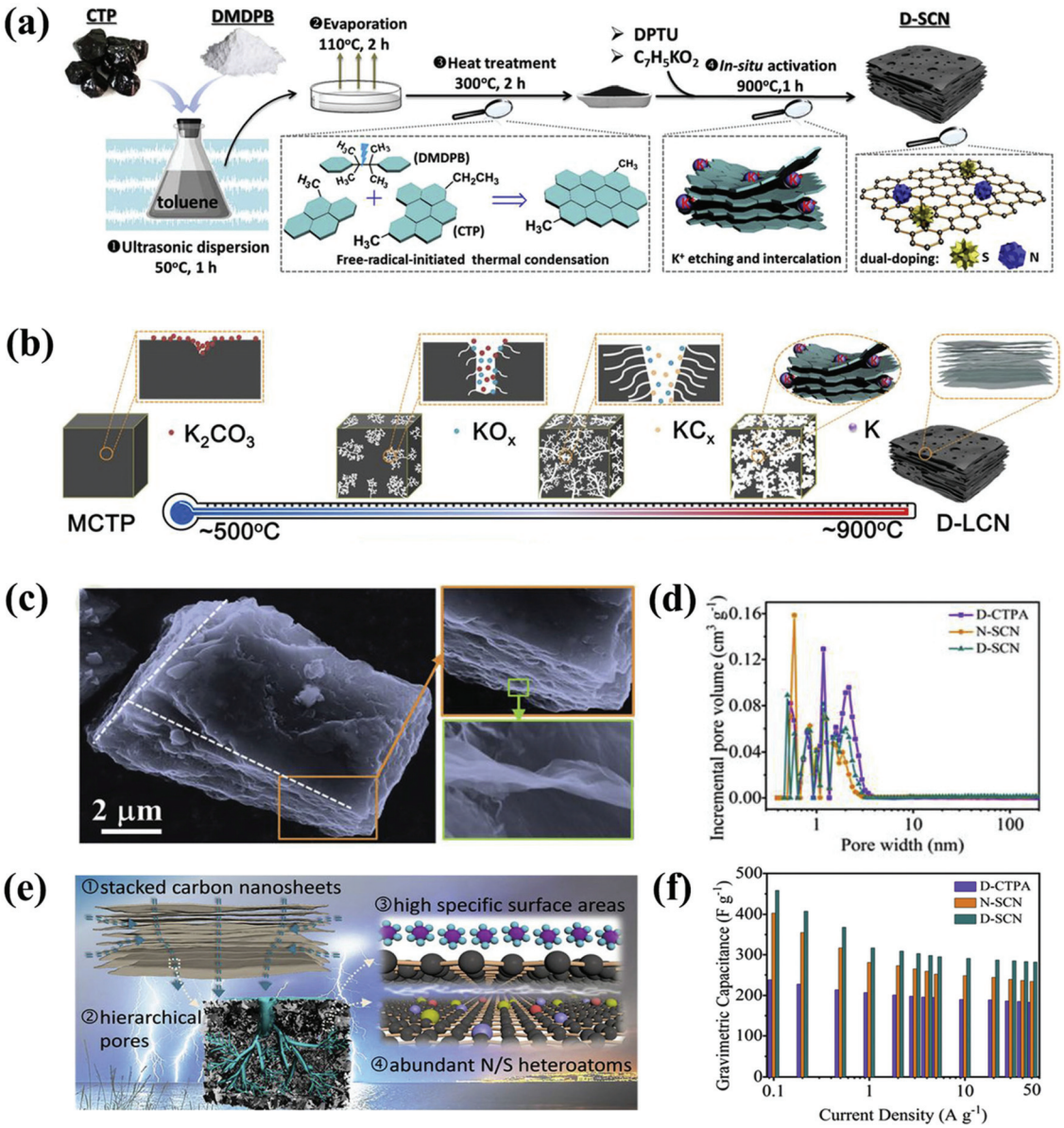

Fig. 13 (a) Proposed synthetic protocol for D-SCN from CTP. (b) A plausible formation mechanism for the nanosheets of SCN. (c) SEM images of D-SCN. (d) The pore size distribution curves of D-CTPA, N-SCN and D-SCN. (e) Schematic of the multi-scale features of D-SCN. (f) Specific capacitance at different current densities. Reproduced with permission from ref. 68. Copyright 2020, Elsevier.

assium evaporated at ~900 °C, leading to the rearrangement of sp^3 carbon structures and generation of sp^2 carbon structures. Fig. 13c demonstrates the desirable interconnected layer-stacked architecture of D-SCN and regular contour lines could also be observed. The pore size distribution curves illustrated that the porous carbon materials possessed abundant micropores and small mesopores between 2 and 5 nm (Fig. 13d). D-SCN exhibited a high SSA of 2285 $m^2\ g^{-1}$ and a V_t of 1.11 $cm^3\ g^{-1}$. The multi-scale features of D-SCN (Fig. 13e) contributed to good capacitance performance. The C_{sp} of D-SCN reached 458 F g^{-1} at 0.1 A g^{-1} and maintained 282 F g^{-1} at 50 A g^{-1} in 2 M KCl electrolyte (Fig. 13f), thus revealing an acceptable rate performance. D-SCN showed a high packing density of 0.78 g cm^{-3}, contributing to the maximum volumetric capacitance of 288 F cm^{-3} at 0.4 A cm^{-3}, which was twice as high as that of commercial activated carbons (~138 F cm^{-3}) and much higher than those of other carbon materials (60–100 F cm^{-3}).

7. Summary and outlook

PCNs are promising electrode materials for supercapacitors, as a result of their high SSAs, tunable porosity and good stability. Chemical activation is an effective strategy to enhance the capacitance performance of PCNs. Traditional activation agents including KOH and $ZnCl_2$ are corrosive and cause severe environmental problems. OPSs are good candidates to replace KOH and $ZnCl_2$ owing to the low corrosive nature of self-generated K_2CO_3. The *in situ* formed molecularly dispersed K_2CO_3 exhibits a good activation effect to produce PCNs with high SSAs above 3000 $m^2\ g^{-1}$ and C_{sp} above 300 F g^{-1}. Although much progress has been made in the OPS-based synthesis of PCNs for supercapacitors, there are some key issues and challenges that need to be solved.

(1) The pore formation mechanisms have not been fully revealed and need further exploration. At present, PCNs obtained from OPS-based synthesis processes always show relatively wide pore size distributions. The ratio among micro-, meso- and macro-pores is not fully optimized and hard to control. From the point of view of volumetric performance and tap density, PCNs with a high ratio of well-developed large micropores (>0.7 nm) and small mesopores (2 nm to 10 nm) are preferred. However, the design of PCNs with fine-tuned pore sizes is still highly challenging. The porosity of PCNs obtained from OPS-based synthesis processes is greatly influenced by many factors, including pyrolysis temperature, heating rate, holding time, and the mass ratio between OPSs and other reagents. At present, only limited research has studied some of these issues on the porosity and capacitance performance of PCNs. More systematic research is needed to probe the intricate relationships between these issues. *In situ*/*operando* characterization techniques to monitor the dynamic morphologies and microstructural changes during the carbonization process will be highly beneficial for revealing the pore formation mechanisms. It will be more efficient to optimize the porosity of PCNs by revealing the pore formation mechanisms. New strategies for producing PCNs with well-controlled pore sizes through more cost-effective and efficient approaches are desired. The template method is still the most effective approach to generate a uniform pore size distribution. Combining OPSs with new templates that display well-controlled architectures and more effective template-removal methods would provide scalable and low-cost approaches for the production of PCNs with well-controlled porosity.

(2) The conductivity of PCNs needs to be improved. To date, most PCNs obtained from OPS-based syntheses are amorphous carbonaceous products with relatively low conductivity (<1 S cm^{-1}) and limited rate performance. Graphitic PCNs should be designed to improve the conductivity and rate performance. Introducing appropriate transition metal salts (*e.g.*, Fe/Co/Ni salts) into the recipe is a good strategy, since carbothermic reduced transition metals show a good catalytic graphitization effect on amorphous carbon. Double salts or complex salts of potassium and transition metals with carbon-rich anions (*e.g.*, citrate, gluconate, alginate) are preferred since the anion derived carbon will restrict the size of carbothermic reduced metal nanoparticles, resulting in evenly distributed nanopores after the acid etching of metal nanoparticles. Therefore, the introduction of transition metal salts will not only enhance the conductivity of PCNs, but also increase the ratio of mesopores. Introducing CNTs and GENSs into the recipe is another good strategy to improve the conductivity of PCNs. CNTs and GENSs themselves exhibit good conductivity and could form a three-dimensional conductive network in PCNs. Moreover, CNTs and GENSs also show a good catalytic graphitization effect and template effect. CNTs could be *in situ* grown on the surface of PCNs by controlling the pyrolysis process of carbon-rich organic double salts or complex salts of potassium and transition metals with (or without) additional carbon sources. An as formed seamlessly connected CNT/PCN hybrid would exhibit greatly enhanced conductivity and a hierarchical architecture that could inhibit the aggregation of PCNs and provide more available surface area to form the EDLC.

(3) Quite a few carbon precursors are products of the petrochemical industry, which are energy-consuming and non-renewable. There is an urgent need to explore sustainable carbon sources. Natural products, especially bio-wastes, deserve to be fully utilized. Most natural products are rich in carbon and could be converted into carbonaceous materials by direct pyrolysis. Natural products always possess a hierarchical pore architecture that can be inherited by the corresponding carbonaceous products. The hierarchical pore architecture is beneficial for the rapid transfer of electrolyte. The microstructures of PCNs could be further tuned by introducing OPSs as the activation agents. At present, potassium citrate and potassium humate are the two most used OPSs for the synthesis of high capacitance PCNs. The exploration of other biomass derived OPSs, like potassium alginate, potassium gluconate, and potassium phytate, for the synthesis of PCNs is of practical significance. Some natural products possess a considerable number of heteroatoms (*e.g.*, N, O, S, P), which can contribute

appreciable pseudocapacitance to the resulting PCNs. Heteroatom-containing precursors are good candidates to synthesize heteroatom doped PCNs with a high heteroatom content and uniform distribution. For example, amino acid derived OPSs are ideal precursors for the production of N-doped PCNs and N,S-codoped PCNs (from cysteine or methionine).

(4) Free-standing electrode materials need to be explored. At present, most PCN products from OPS-based synthesis are powders. The preparation of electrodes requires the addition of a conductive agent and polymer binder, which increases the "dead volume/weight" of electrodes and reduces the rate performance. Therefore, it is meaningful to design free-standing electrode materials to improve the rate performance and power density of supercapacitors, especially for flexible and wearable devices. Nanotechnologies including wet spinning, electrospinning, and film casting, are effective approaches to generate free-standing carbon nanomaterials. For example, an activated carbon nanofiber membrane could be obtained by the carbonization of an electrospun lignin nanofiber membrane, which undergoes cation exchange with potassium ions. Activated carbon microfibers could be produced by the carbonization the hybrid microfibers of biopolymers (*e.g.*, cellulose, chitosan, starch, protein) and OPSs. Carbon aerogel could be synthesized from the carbonization of potassium alginate aerogel or hybrid aerogels of biopolymer and OPSs prepared *via* film casting. Free-standing PCNs could also be produced from other facile "top-down" approaches. For example, activated carbon fiber cloth could be obtained by the one-step carbonization and activation of cotton fiber cloth loaded with OPSs *via* a "dip and dry" process.

Conflicts of interest

The authors declare that they have no conflict of interest.

Acknowledgements

Dr S. He gratefully acknowledges financial support from the National Natural Science Foundation of China (No. 22005147). Dr B. You acknowledges financial support from the Start-up Funding of the Huazhong University of Science and Technology (HUST) and the Program for HUST Academic Frontier Youth Team (2018QYTD15). Dr X. Zhao acknowledges financial support from the Wuhan University of Technology Startup Fund (40120562).

Notes and references

1 H. Shao, Y.-C. Wu, Z. Lin, P.-L. Taberna and P. Simon, *Chem. Soc. Rev.*, 2020, **49**, 3005–3039.
2 W. Tian, H. Zhang, X. Duan, H. Sun, G. Shao and S. Wang, *Adv. Funct. Mater.*, 2020, **30**, 1909265.
3 X. Tang, D. Liu, Y.-J. Wang, L. Cui, A. Ignaszak, Y. Yu and J. Zhang, *Prog. Mater. Sci.*, 2021, **118**, 100770.
4 P. Xie, W. Yuan, X. Liu, Y. Peng, Y. Yin, Y. Li and Z. Wu, *Energy Storage Mater.*, 2021, **36**, 56–76.
5 H. Shi, G. Wen, Y. Nie, G. Zhang and H. Duan, *Nanoscale*, 2020, **12**, 5261–5285.
6 U. Kamran and S. J. Park, *J. Cleaner Prod.*, 2021, **290**, 125776.
7 U. Kamran, Y. J. Heo, J. W. Lee and S. J. Park, *Micromachines*, 2019, **10**, 234.
8 K. A. Cychosz, R. Guillet-Nicolas, J. Garcia-Martinez and M. Thommes, *Chem. Soc. Rev.*, 2017, **46**, 389–414.
9 M. Thommes, K. Kaneko, A. V. Neimark, J. P. Olivier, F. Rodriguez-Reinoso, J. Rouquerol and K. S. W. Sing, *Pure Appl. Chem.*, 2015, **87**, 1051–1069.
10 T. Y. Liu, F. Zhang, Y. Song and Y. Li, *J. Mater. Chem. A*, 2017, **5**, 17705–17733.
11 J. Yin, W. Zhang, N. A. Alhebshi, N. Salah and H. N. Alshareef, *Small Methods*, 2020, **4**, 1900853.
12 X. Chu, F. Meng, T. Deng and W. Zhang, *Nanoscale*, 2021, **13**, 5570–5593.
13 F. Wang, J. Y. Cheong, J. Lee, J. Ahn, G. Duan, H. Chen, Q. Zhang, I.-D. Kim and S. Jiang, *Adv. Funct. Mater.*, 2021, **31**, 2101077.
14 H. Wang, Y. Shao, S. Mei, Y. Lu, M. Zhang, J.-K. Sun, K. Matyjaszewski, M. Antonietti and J. Yuan, *Chem. Rev.*, 2020, **120**, 9363–9419.
15 Z. Li, D. Guo, Y. Liu, H. Wang and L. Wang, *Chem. Eng. J.*, 2020, **397**, 125418.
16 M. R. Benzigar, S. N. Talapaneni, S. Joseph, K. Ramadass, G. Singh, J. Scaranto, U. Ravon, K. Al-Bahily and A. Vinu, *Chem. Soc. Rev.*, 2018, **47**, 2680–2721.
17 F. Wang, J. Y. Cheong, Q. He, G. Duan, S. He, L. Zhang, Y. Zhao, I.-D. Kim and S. Jiang, *Chem. Eng. J.*, 2021, **414**, 128767.
18 Q. Du, Y. Zhao, K. Zhuo, Y. Chen, L. Yang, C. Wang and J. Wang, *Nanoscale*, 2021, **13**, 13285–13293.
19 F. Wang, X. Liu, G. Duan, H. Yang, J. Y. Cheong, J. Lee, J. Ahn, Q. Zhang, S. He, J. Han, Y. Zhao, I.-D. Kim and S. Jiang, *Small*, 2021, **17**, 2102532.
20 H. Li, L. Cao, F. Wang, G. Duan, W. Xu, C. Mei, G. Zhang, K. Liu, M. Yang and S. Jiang, *Front. Chem.*, 2020, **8**, 00089.
21 J. Chen, Y. Lin, J. Liu, D. Wu, X. Bai, D. Chen and H. Li, *J. Energy Storage*, 2021, **39**, 102640.
22 J. Du, L. Liu, H. Wu and A. Chen, *Nanoscale*, 2019, **11**, 22796–22803.
23 M. Yuan, T. Liu, Q. Shi and J. Dong, *Chem. Eng. J.*, 2021, **428**, 132016.
24 S. Zhu, N. Zhao, J. Li, X. Deng, J. Sha and C. He, *Nano Today*, 2019, **29**, 100796.
25 N. Díez, M. Sevilla and A. B. Fuertes, *Carbon*, 2021, **178**, 451–476.
26 B. Yan, W. Zhang, X. Qin, Y. Choi, G. Diao, X. Jin and Y. Piao, *Chem. Eng. J.*, 2020, **400**, 125895.
27 T. Y. Kou, B. Yao, T. Y. Liu and Y. Li, *J. Mater. Chem. A*, 2017, **5**, 17151.

28 Y. He, X. Zhuang, C. Lei, L. Lei, Y. Hou, Y. Mai and X. Feng, *Nano Today*, 2019, **24**, 103–119.
29 Y. Chen, X. Hao and G. Z. Chen, *Energy Environ. Mater.*, 2020, **3**, 247–264.
30 L. Miao, Z. Song, D. Zhu, L. Li, L. Gan and M. Liu, *Mater. Adv.*, 2020, **1**, 945–966.
31 C. Young, T. Park, J. W. Yi, J. Kim, M. S. A. Hossain, Y. V. Kaneti and Y. Yamauchi, *ChemSusChem*, 2018, **11**, 3546–3558.
32 J. Wang, Y. Wang, H. Hu, Q. Yang and J. Cai, *Nanoscale*, 2020, **12**, 4238–4268.
33 J. Jjagwe, P. W. Olupot, E. Menya and H. M. Kalibbala, *J. Bioresour. Bioprod.*, 2021, **6**, 292–322.
34 U. Kamran and S. J. Park, *J. Colloid Interface Sci.*, 2021, **594**, 745–758.
35 U. Kamran, J. R. Choi and S.-J. Park, *Front. Chem.*, 2020, **8**, 710.
36 X. Wei and T. Li, *ACS Omega*, 2021, **6**, 5607–5618.
37 Y. Yoshikawa, K. Teshima, R. Futamura, H. Tanaka, A. V. Neimark and K. Kaneko, *J. Colloid Interface Sci.*, 2020, **578**, 422–430.
38 Suhas, V. K. Gupta, L. P. Singh, M. Chaudhary and S. Kushwaha, *J. Cleaner Prod.*, 2021, **288**, 125643.
39 R. Cai, Y. Si, B. You, M. Chen and L. Wu, *ACS Appl. Mater. Interfaces*, 2020, **12**, 28738–28749.
40 P. Nai Yuh Yek, C. Li, W. Peng, C. Swee Wong, R. Keey Liew, W. Adibah Wan Mahari, C. Sonne and S. Shiung Lam, *Chem. Eng. J.*, 2021, **425**, 131886.
41 S. S. Gunasekaran and S. Badhulika, *J. Energy Storage*, 2021, **41**, 102997.
42 B. A. Goodman, *J. Bioresour. Bioprod.*, 2020, **5**, 143–162.
43 D. A. Khuong, H. N. Nguyen and T. Tsubota, *Biomass Bioenergy*, 2021, **148**, 106039.
44 S. Y. Hwang, C.-H. Lee, H. Ri Lee, S.-Y. Son, S. Lee and H.-I. Joh, *Chem. Eng. Sci.*, 2021, **231**, 116301.
45 S. S. Lam, P. N. Y. Yek, Y. S. Ok, C. C. Chong, R. K. Liew, D. C. W. Tsang, Y.-K. Park, Z. Liu, C. S. Wong and W. Peng, *J. Hazard. Mater.*, 2020, **390**, 121649.
46 Y. Wang, Q. Qu, S. Gao, G. Tang, K. Liu, S. He and C. Huang, *Carbon*, 2019, **155**, 706–726.
47 C. Jiang, G. A. Yakaboylu, T. Yumak, J. W. Zondlo, E. M. Sabolsky and J. Wang, *Renewable Energy*, 2020, **155**, 38–52.
48 L. Xiong, X.-F. Wang, L. Li, L. Jin, Y.-G. Zhang, S.-L. Song and R.-P. Liu, *Energy Fuels*, 2019, **33**, 12558–12567.
49 Y. Zhang, L. Chen, S. Mao, Z. Sun, Y. Song and R. Zhao, *J. Colloid Interface Sci.*, 2019, **536**, 252–260.
50 W. Yang, H. Chen, X. Han, S. Ding, Y. Shan and Y. Liu, *J. Hazard. Mater.*, 2020, **381**, 120981.
51 W. Xu, K. Sun, C. Miao, A. Wang, Y. Song and J. Liu, *J. For. Eng.*, 2018, **3**, 40–46.
52 A. B. Fuertes, G. A. Ferrero and M. Sevilla, *J. Mater. Chem. A*, 2014, **2**, 14439–14448.
53 D. Puthusseri, V. Aravindan, S. Madhavi and S. Ogale, *Energy Environ. Sci.*, 2014, **7**, 728–735.
54 M. Sevilla and A. B. Fuertes, *ACS Nano*, 2014, **8**, 5069–5078.
55 Z. J. Zhang, X. Y. Chen, D. H. Xie, P. Cui and J. W. Liu, *J. Mater. Chem. A*, 2014, **2**, 9675–9683.
56 H. Luo, Y. Yang, X. Zhao, J. Zhang and Y. Chen, *Electrochim. Acta*, 2015, **169**, 13–21.
57 Y. Jiang, J. Yan, X. Wu, D. Shan, Q. Zhou, L. Jiang, D. Yang and Z. Fan, *J. Power Sources*, 2016, **307**, 190–198.
58 J. Zhang, W. Zhang, H. Zhang, J. Pang, G. Cao, M. Han and Y. Yang, *J. Alloys Compd.*, 2017, **712**, 76–81.
59 K. Jayaramulu, D. P. Dubal, B. Nagar, V. Ranc, O. Tomanec, M. Petr, K. K. R. Datta, R. Zboril, P. Gomez-Romero and R. A. Fischer, *Adv. Mater.*, 2018, **30**, e1705789.
60 Y. Zhang, Q. Ma, H. Li, Y. W. Yang and J. Luo, *Small*, 2018, **14**, e1800133.
61 X. Li, J. Zhou, L. Xu, M. Wang and X. Li, *Appl. Surf. Sci.*, 2019, **490**, 604–610.
62 S. Sun, B. Ding, R. Liu and X. Wu, *J. Alloys Compd.*, 2019, **803**, 401–406.
63 D. Wang, J. Nai, L. Xu and T. Sun, *ACS Sustainable Chem. Eng.*, 2019, **7**, 18901–18911.
64 G. Huang, Q. Geng, W. Kang, Y. Liu, Y. Li, B. Xing, Q. Liu and C. Zhang, *Microporous Mesoporous Mater.*, 2019, **288**, 109576.
65 J. Zhou, L. Jiang, C. Shu, L. Kong, I. Ahmad, Y. N. Zhou, W. Tang, X. Sun and Y. Wu, *Energy Environ. Mater.*, 2020, 1–8.
66 M. Zhou, Y. Lin, H. Xia, X. Wei, Y. Yao, X. Wang and Z. Wu, *Nano-Micro Lett.*, 2020, **12**, 58.
67 J. M. Li, Q. M. Jiang, L. S. Wei, L. X. Zhong and X. Y. Wang, *J. Mater. Chem. A*, 2020, **8**, 1469–1479.
68 G. L. Zhang, T. T. Guan, J. L. Qiao, J. L. Wang and K. X. Li, *Energy Storage Mater.*, 2020, **26**, 119–128.
69 L. Hou, W. Yang, Y. Li, P. Wang, B. Jiang, C. Xu, C. Zhang, G. Huang, F. Yang and Y. Li, *Chem. Eng. J.*, 2021, **417**, 129289.
70 T. Liu, Y. Lan, Q. Zhu, G. Du, X. Su and Z. Lin, *Chem. Eng. J.*, 2021, **421**, 129993.
71 G. Yuan, K. X. Guan, H. Hu, B. F. Lei, Y. Xiao, H. W. Dong, Y. R. Liang, Y. L. Liu and M. T. Zheng, *J. Colloid Interface Sci.*, 2021, **582**, 159–166.
72 W. Yang, P. Wang, Z. Tu, L. Hou, L. Yan, B. Jiang, C. Zhang, G. Huang, F. Yang and Y. Li, *Carbon*, 2022, **187**, 338–348.
73 D. W. Kim, H. S. Kil, K. Nakabayashi, S. H. Yoon and J. Miyawaki, *Carbon*, 2017, **114**, 98–105.
74 J. Wang and S. Kaskel, *J. Mater. Chem.*, 2012, **22**, 23710.
75 S. Zheng, J. Zhang, H. Deng, Y. Du and X. Shi, *J. Bioresour. Bioprod.*, 2021, **6**, 142–151.
76 N. Díez, A. B. Fuertes and M. Sevilla, *Energy Storage Mater.*, 2021, **38**, 50–69.
77 M. R. Saeb, N. Rabiee, F. Seidi, B. Farasati Far, M. Bagherzadeh, E. C. Lima and M. Rabiee, *J. Bioresour. Bioprod.*, 2021, **6**, 215–222.
78 Y. Su, S. Liu, G. Ye, W. Zhu, K. Zhao, R. Huang and Z. He, *ACS Appl. Energy Mater.*, 2021, **4**, 5375–5380.
79 G. Guo, S. Ma, X. Hu, J. Fu, W. Xu, K. Huang and J. Zou, *J. For. Eng.*, 2020, **5**, 106–113.

80 M. Kim, X. Xu, R. Xin, J. Earnshaw, A. Ashok, J. Kim, T. Park, A. K. Nanjundan, W. A. El-Said, J. W. Yi, J. Na and Y. Yamauchi, *ACS Appl. Mater. Interfaces*, 2021, **13**, 52034–52043.
81 X. Jian, X. Hou, W. Xu and S. Liu, *J. For. Eng.*, 2021, **6**, 114–119.
82 U. Kamran and S.-J. Park, *J. CO_2 Util.*, 2020, **40**, 101212.
83 R. Li, Z. Lou, S. Gu, Q. Wang, J. Liu and Y. Li, *J. For. Eng.*, 2021, **6**, 112–120.
84 Z. Wang, C. Hu, D. Tu, W. Zhang and L. Guan, *J. For. Eng.*, 2020, **5**, 96–102.
85 Z. Pan, Z. Lu, L. Xu and D. Wang, *Appl. Surf. Sci.*, 2020, **510**, 145384.
86 H. Zhang, X. He, F. Wei, S. Dong, N. Xiao and J. Qiu, *ACS Sustainable Chem. Eng.*, 2020, **8**, 3065–3071.
87 A. R. Selvaraj, A. Muthusamy, C. Inho, H.-J. Kim, K. Senthil and K. Prabakar, *Carbon*, 2021, **174**, 463–474.
88 N. Sangtong, T. Chaisuwan, S. Wongkasemjit, H. Ishida, W. Redpradit, K. Seneesrisakul and U. Thubsuang, *Microporous Mesoporous Mater.*, 2021, **326**, 111383.
89 S. Chen, S. Jiang and H. Jiang, *J. Bioresour. Bioprod.*, 2020, **5**, 238–247.
90 Z. Lou, W. Wang, C. Yuan, Y. Zhang, Y. Li and L. Yang, *J. Bioresour. Bioprod.*, 2019, **4**, 43–50.
91 Z. Han, W. Zhong and K. Wang, *J. For. Eng.*, 2020, **5**, 76–83.
92 A. G. M. Shoaib, A. El-Sikaily, A. El Nemr, A. E.-D. A. Mohamed and A. A. Hassan, *Biomass Convers. Biorefin.*, 2022, **12**, 2253–2265.
93 H. Nassar, A. Zyoud, A. El-Hamouz, R. Tanbour, N. Halayqa and H. S. Hilal, *Sustainable Chem. Pharm.*, 2020, **18**, 100335.
94 X. Xing, W. Jiang, S. Li, X. Zhang and W. Wang, *Waste Manage.*, 2019, **89**, 64–72.
95 M. Sevilla and A. B. Fuertes, *ChemSusChem*, 2016, **9**, 1880–1888.
96 Y. Li, Z. Li, B. Xing, H. Li, Z. Ma, W. Zhang, P. Reubroycharoen and S. Wang, *J. Anal. Appl. Pyrolysis*, 2021, **155**, 105072.
97 Q. Luo, Q. Chen, Y. Wang, Y. Long, W. Jiang and G. Fan, *Chem. Eng. J.*, 2021, **420**, 130483.
98 B. Yang, J. Chen, L. Liu, P. Ma, B. Liu, J. Lang, Y. Tang and X. Yan, *Energy Storage Mater.*, 2019, **23**, 522–529.
99 J. Deng, P. Ren, D. Deng and X. Bao, *Angew. Chem., Int. Ed.*, 2015, **54**, 2100–2104.
100 C. X. Lv, W. J. Xu, H. L. Liu, L. X. Zhang, S. Chen, X. F. Yang, X. J. Xu and D. J. Yang, *Small*, 2019, **15**(23), 1900816.
101 W. T. Feng, Y. P. Cui, W. Liu, H. L. Wang, Y. Zhang, Y. X. Du, S. Liu, H. L. Wang, X. Gao and T. Q. Wang, *ACS Nano*, 2020, **14**, 4938–4949.
102 H. Cheng, Y. Song, Y. R. Bian, R. T. Ji, F. Wang, C. G. Gu, X. L. Yang, M. Ye, G. F. Ouyang and X. Jiang, *Sci. Total Environ.*, 2019, **681**, 392–399.
103 Y. M. Zhang, Z. P. Wang, D. P. Li, Q. Sun, K. R. Lai, K. K. Li, Q. H. Yuan, X. J. Liu and L. J. Ci, *J. Mater. Chem. A*, 2020, **8**, 22874–22885.
104 D. W. Wang, G. X. Chen and Z. M. Pan, *Nanotechnology*, 2021, **32**(18), 185403.
105 H. Luo, W.-J. Jiang, Y. Zhang, S. Niu, T. Tang, L.-B. Huang, Y.-Y. Chen, Z. Wei and J.-S. Hu, *Carbon*, 2018, **128**, 97–105.
106 T. Wu, C. Zhang, H. Hou, P. Ge, G. Zou, W. Xu, S. Li, Z. Huang, T. Guo, M. Jing and X. Ji, *Adv. Funct. Mater.*, 2018, **28**, 1705744.
107 W. Chen, C. Chen, X. Xiong, P. Hu, Z. Hao and Y. Huang, *Adv. Sci.*, 2017, **4**, 1600500.
108 P. Xiong, J. Wu, M. Zhou and Y. Xu, *ACS Nano*, 2020, **14**, 1018–1026.
109 X.-D. He, Z.-H. Liu, J.-Y. Liao, X. Ding, Q. Hu, L.-N. Xiao, S. Wang and C.-H. Chen, *J. Mater. Chem. A*, 2019, **7**, 9629–9637.
110 M. Sevilla and A. B. Fuertes, *J. Mater. Chem. A*, 2013, **1**, 13738–13741.
111 L. Hou, W. Yang, B. Jiang, P. Wang, L. Yan, C. Zhang, G. Huang, F. Yang and Y. Li, *Carbon*, 2021, **183**, 176–186.
112 J. Lee, Y. A. Lee, C. Y. Yoo, J. J. Yoo, R. Gwak, W. K. Cho, B. Kim and H. Yoon, *Microporous Mesoporous Mater.*, 2018, **261**, 119–125.
113 M. Sevilla, G. A. Ferrero, N. Diez and A. B. Fuertes, *Carbon*, 2018, **131**, 193–200.
114 L. He, W. C. Li, S. Xu and A. H. Lu, *Chem. – Eur. J.*, 2019, **25**, 3209–3218.
115 L. Borchardt, Q.-L. Zhu, M. E. Casco, R. Berger, X. Zhuang, S. Kaskel, X. Feng and Q. Xu, *Mater. Today*, 2017, **20**, 592–610.
116 Y. Q. Zhu, T. Cao, C. B. Cao, J. Luo, W. X. Chen, L. R. Zheng, J. C. Dong, J. Zhang, Y. H. Han, Z. Li, C. Chen, Q. Peng, D. S. Wang and Y. D. Li, *ACS Catal.*, 2018, **8**, 10004–10011.
117 J. S. Byun, Y. Chan Jeong, J. H. Kim, M. Chang Shin, J. Y. Park, H.-J. Jin, C. R. Park, T. Kim and S. J. Yang, *Carbon*, 2020, **173**, 637–645.
118 Z. Y. Wu, S. L. Xu, Q. Q. Yan, Z. Q. Chen, Y. W. Ding, C. Li, H. W. Liang and S. H. Yu, *Sci. Adv.*, 2018, **4**, eaat0788.
119 L. C. Xia, H. Huang, Z. Fan, D. W. Hu, D. M. Zhang, A. S. Khan, M. Usman and L. J. Pan, *Mater. Des.*, 2019, **182**, 108048.
120 Y. Zhao, Y. Yuan, Y. Xu, G. Zheng, Q. Zhang, Y. Jiang, Z. Wang, N. Bu, L. Xia and Z. Yan, *Nanoscale*, 2021, **13**, 1961–1969.
121 W. Yang, L. Dong, W. Yang, C. Xu, G. Shao and G. Wang, *Small Methods*, 2019, **4**, 1900670.
122 C. Zhao, Z. Hu and J. Luo, *Colloids Surf., A*, 2019, **560**, 69–77.
123 A. C. Dassanayake and M. Jaroniec, *J. Mater. Chem. A*, 2017, **5**, 19456–19466.
124 L. Hu, Y. Lu, X. Li, J. Liang, T. Huang, Y. Zhu and Y. Qian, *Small*, 2017, **13**, 1603533.
125 Y. Hou, J. Li, X. Gao, Z. Wen, C. Yuan and J. Chen, *Nanoscale*, 2016, **8**, 8228–8235.
126 L. Zhao, Y. Zhang, L. B. Huang, X. Z. Liu, Q. H. Zhang, C. He, Z. Y. Wu, L. J. Zhang, J. Wu, W. Yang, L. Gu, J. S. Hu and L. J. Wan, *Nat. Commun.*, 2019, **10**, 1278.

127 M. Sevilla, G. A. Ferrero and A. B. Fuertes, *Chem. Mater.*, 2017, **29**, 6900–6907.
128 X. Tong, Z. Chen, H. Zhuo, Y. Hu, S. Jing, J. Liu and L. Zhong, *Carbohydr. Polym.*, 2019, **207**, 764–774.
129 F. Zhang, H. Liu, Z. Wu, J. Zhang, E. Cui, L. Yue and G. Hou, *ACS Appl. Energy Mater.*, 2021, **4**, 6719–6729.
130 L. Wang, F. Sun, F. Hao, Z. Qu, J. Gao, M. Liu, K. Wang, G. Zhao and Y. Qin, *Chem. Eng. J.*, 2020, **383**, 123205.
131 J. Xia, N. Zhang, S. Chong, D. Li, Y. Chen and C. Sun, *Green Chem.*, 2018, **20**, 694–700.
132 F. Wei, X. He, L. Ma, H. Zhang, N. Xiao and J. Qiu, *Nano-Micro Lett.*, 2020, **12**, 82.
133 Y. Wang, Y. Song and Y. Xia, *Chem. Soc. Rev.*, 2016, **45**, 5925–5950.
134 P. Simon and Y. Gogotsi, *Nat. Mater.*, 2020, **19**, 1151–1163.
135 S. He and W. Chen, *Nanoscale*, 2015, **7**, 6957–6990.
136 T. Q. Lin, I. W. Chen, F. X. Liu, C. Y. Yang, H. Bi, F. F. Xu and F. Q. Huang, *Science*, 2015, **350**, 1508–1513.
137 B. Yan, J. Zheng, F. Wang, L. Zhao, Q. Zhang, W. Xu and S. He, *Mater. Des.*, 2021, **201**, 109518.
138 P. Simon and Y. Gogotsi, *Acc. Chem. Res.*, 2013, **46**, 1094–1103.
139 G. Feng and P. T. Cummings, *J. Phys. Chem. Lett.*, 2011, **2**, 2859–2864.
140 C. Largeot, C. Portet, J. Chmiola, P. L. Taberna, Y. Gogotsi and P. Simon, *J. Am. Chem. Soc.*, 2008, **130**, 2730–2731.
141 P. Simon and Y. Gogotsi, *Nat. Mater.*, 2008, **7**, 845–854.
142 F. Zhang, T. Y. Liu, M. Y. Li, M. H. Yu, Y. Luo, Y. X. Tong and Y. Li, *Nano Lett.*, 2017, **17**, 3097–3104.
143 G. Ramos-Fernández, M. Canal-Rodríguez, A. Arenillas, J. A. Menéndez, I. Rodríguez-Pastor and I. Martin-Gullon, *Carbon*, 2018, **126**, 456–463.
144 H. L. Fan and W. Z. Shen, *ACS Sustainable Chem. Eng.*, 2016, **4**, 1328–1337.
145 G. P. Hao, A. H. Lu, W. Dong, Z. Y. Jin, X. Q. Zhang, J. T. Zhang and W. C. Li, *Adv. Energy Mater.*, 2013, **3**, 1421–1427.
146 J. J. Zhang, H. P. Zhao, J. Li, H. L. Jin, X. C. Yu, Y. Lei and S. Wang, *Adv. Energy Mater.*, 2019, **9**, 1803221.
147 Y. L. Zhao and X. H. Zhang, *Sci. Rep.*, 2021, **11**, 6825.
148 B. B. Chang, W. W. Shi, S. C. Han, Y. N. Zhou, Y. X. Liu, S. R. Zhang and B. C. Yang, *Chem. Eng. J.*, 2018, **350**, 585–598.
149 Y. L. Wen, L. Chi, X. Wen, X. C. Chen and E. Mijowska, *Adv. Electron. Mater.*, 2020, **6**, 2000450.
150 C. Li, X. Zhang, K. Wang, X. Sun, G. Liu, J. Li, H. Tian, J. Li and Y. Ma, *Adv. Mater.*, 2017, **29**, 1604690.
151 S. Zhang, X. Z. Shi, X. Wen, X. C. Chen, P. K. Chu, T. Tang and E. Mijowska, *J. Power Sources*, 2019, **435**, 226811.
152 B. Liu, M. Yang, H. B. Chen, Y. J. Liu, D. G. Yang and H. M. Li, *J. Power Sources*, 2018, **397**, 1–10.
153 Y. J. Li, G. Zhu, H. L. Huang, M. Xu, T. Lu and L. K. Pan, *J. Mater. Chem. A*, 2019, **7**, 9040–9050.
154 F. Wang, X. L. Liu, G. G. Duan, H. Q. Yang, J. Y. Cheong, J. Lee, J. Ahn, Q. Zhang, S. J. He, J. Q. Han, Y. Zhao, I. D. Kim and S. H. Jiang, *Small*, 2021, **17**, 2102532.
155 Y. Qing, Y. T. Jiang, H. Lin, L. X. Wang, A. J. Liu, Y. L. Cao, R. Sheng, Y. Guo, C. W. Fan, S. Zhang, D. Z. Jia and Z. J. Fan, *J. Mater. Chem. A*, 2019, **7**, 6021–6027.
156 F. Cheng, X. P. Yang, S. P. Zhang and W. Lu, *J. Power Sources*, 2020, **450**, 227678.
157 R. J. Lin, Z. N. Li, D. I. Abou El Amaiem, B. J. Zhang, D. J. L. Brett, G. J. He and I. P. Parkin, *J. Mater. Chem. A*, 2017, **5**, 25545–25554.
158 X. Li, Y. Tang, J. H. Song, W. Yang, M. S. Wang, C. Z. Zhu, W. G. Zhao, J. M. Zheng and Y. H. Lin, *Carbon*, 2018, **129**, 236–244.
159 G. H. Xu, C. Zheng, Q. Zhang, J. Q. Huang, M. Q. Zhao, J. Q. Nie, X. H. Wang and F. Wei, *Nano Res.*, 2011, **4**, 870–881.
160 X. J. Lu, H. Dou, B. Gao, C. Z. Yuan, S. D. Yang, L. Hao, L. F. Shen and X. G. Zhang, *Electrochim. Acta*, 2011, **56**, 5115–5121.
161 H. Y. Chen, S. Zeng, M. H. Chen, Y. Y. Zhang and Q. W. Li, *Carbon*, 2015, **92**, 271–296.
162 Y. Wang, Q. Qu, J. Cui, T. Lu, F. Li, M. Zhang, K. Liu, Q. Zhang, S. He and C. Huang, *Carbohydr. Polym. Technol. Appl.*, 2021, **2**, 100117.
163 F. Wang, L. Chen, H. Li, G. Duan, S. He, L. Zhang, G. Zhang, Z. Zhou and S. Jiang, *Chin. Chem. Lett.*, 2020, **31**, 1986–1990.
164 S. He, C. Zhang, C. Du, C. Cheng and W. Chen, *J. Power Sources*, 2019, **434**, 226701.
165 S. Ghosh, S. Barg, S. M. Jeong and K. Ostrikov, *Adv. Energy Mater.*, 2020, **10**, 2001239.
166 W. J. Lee, J. Lim and S. O. Kim, *Small Methods*, 2017, **1**, 1600014.
167 I. Y. Jeon, H. J. Noh and J. B. Baek, *Chem. – Asian J.*, 2020, **15**, 2282–2293.
168 Y. Deng, Y. Xie, K. Zou and X. Ji, *J. Mater. Chem. A*, 2016, **4**, 1144–1173.
169 F. Sun, Z. B. Qu, J. H. Gao, H. B. Wu, F. Liu, R. Han, L. J. Wang, T. Pei, G. B. Zhao and Y. F. Lu, *Adv. Funct. Mater.*, 2018, **28**, 1804190.
170 S. B. Li, Z. F. Wang, H. M. Jiang, L. M. Zhang, J. Z. Ren, M. T. Zheng, L. C. Dong and L. Y. Sun, *Chem. Commun.*, 2016, **52**, 10988–10991.
171 L. Cao, H. Li, X. Liu, S. Liu, L. Zhang, W. Xu, H. Yang, H. Hou, S. He, Y. Zhao and S. Jiang, *J. Colloid Interface Sci.*, 2021, **599**, 443–452.
172 Y. J. Ma, X. G. Zhang, Z. Liang, C. L. Wang, Y. Sui, B. Zheng, Y. C. Ye, W. J. Ma, Q. Zhao and C. L. Qin, *Electrochim. Acta*, 2020, **337**, 135800.
173 C. X. Cui, Y. Gao, J. Li, C. Yang, M. Liu, H. L. Jin, Z. H. Xia, L. M. Dai, Y. Lei, J. C. Wang and S. Wang, *Angew. Chem., Int. Ed.*, 2020, **59**, 7928–7933.
174 D. Johnsirani and A. Pandurangan, *Diamond Relat. Mater.*, 2020, **105**, 107800.
175 J. E. Zuliani, S. Tong, C. Q. Jia and D. W. Kirk, *J. Power Sources*, 2018, **395**, 271–279.
176 X. W. Wang, C. Yang, J. Li, X. A. Chen, K. Q. Yang, X. C. Yu, D. J. Lin, Q. C. Zhang, S. Wang, J. C. Wang,

Z. H. Xia and H. L. Jin, *Adv. Funct. Mater.*, 2021, **31**, 2009109.
177 Y. Wang, J. Cui, Q. Qu, W. Ma, F. Li, W. Du, K. Liu, Q. Zhang, S. He and C. Huang, *Microporous Mesoporous Mater.*, 2022, **329**, 111545.
178 M. W. Xia, W. Chen, J. Wu, Y. Q. Chen, H. P. Yang, X. Chen, D. C. Zhu and H. P. Chen, *Fuel*, 2021, **291**, 120185.
179 M. Sevilla, G. A. Ferrero and A. B. Fuertes, *Carbon*, 2017, **114**, 50–58.
180 M. Sevilla, A. S. M. Al-Jumialy, A. B. Fuertes and R. Mokaya, *ACS Appl. Mater. Interfaces*, 2018, **10**, 1623–1633.
181 A. B. Ross, C. Hall, K. Anastasakis, A. Westwood, J. M. Jones and R. J. Crewe, *J. Anal. Appl. Pyrolysis*, 2011, **91**, 344–351.
182 L. Wang, Q. Zhu, J. Zhao, Y. Guan, J. Liu, Z. An and B. Xu, *Microporous Mesoporous Mater.*, 2019, **279**, 439–445.
183 X. Wu, B. Ding, C. Zhang, B. Li and Z. Fan, *Carbon*, 2019, **153**, 225–233.
184 L. Wang, M. Huang, J. Huang, X. Tang, L. Li, M. Peng, K. Zhang, T. Hu, K. Yuan and Y. Chen, *J. Mater. Chem. A*, 2021, **9**, 15404–15414.
185 J. Shi, H. Cui, J. Xu, N. Yan, Y. Liu and S. Zhang, *J. CO_2 Util.*, 2020, **39**, 101164.
186 Z. Liu, J. Luo, Y. Peng, Y. Yang, Z. Zeng and L. Li, *Colloids Surf., A*, 2020, **606**, 125431.
187 X. Wang, J. Lu, Y. Zhao, X. Wang, Z. Lin, X. Liu, R. Wu, C. Yang and X. Su, *ChemCatChem*, 2018, **10**, 4143–4153.
188 M.-J. Kim, S. W. Choi, H. Kim, S. Mun and K. B. Lee, *Chem. Eng. J.*, 2020, **397**, 125404.
189 J. Mu, Q. Li, X. Kong, X. Wu, J. Sunarso, Y. Zhao, J. Zhou and S. Zhuo, *ChemElectroChem*, 2019, **6**, 4022–4030.
190 C. Ma, J. Gong, S. Zhao, X. Liu, X. Mu, Y. Wang, X. Chen and T. Tang, *Green Energy Environ.*, 2022, **7**(4), 818–828.
191 C. K. Roy, S. S. Shah, A. H. Reaz, S. Sultana, A.-N. Chowdhury, S. H. Firoz, M. H. Zahir, M. A. Ahmed Qasem and M. A. Aziz, *Chem. – Asian J.*, 2021, **16**, 296–308.
192 M. Sevilla, G. A. Ferrero and A. B. Fuertes, *Chem. Mater.*, 2017, **29**, 6900–6907.
193 H. Lin, C. Xu, Q. Wang, J. Wu, Y. Wang, Y. Zhang and G. Fan, *Int. J. Hydrogen Energy*, 2019, **44**, 21527–21535.
194 J. Ludwinowicz and M. Jaroniec, *Carbon*, 2015, **82**, 297–303.
195 G. Singh, I. S. Ismail, C. Bilen, D. Shanbhag, C. I. Sathish, K. Ramadass and A. Vinu, *Appl. Energy*, 2019, **255**, 113831.
196 J. Dai, S. Tian, Y. Jiang, Z. Chang, A. Xie, R. Zhang and Y. Yan, *J. Alloys Compd.*, 2018, **732**, 222–232.
197 J. Zhang, W. Zhang, M. Han, J. Pang, Y. Xiang, G. Cao and Y. Yang, *Microporous Mesoporous Mater.*, 2018, **270**, 204–210.
198 Q. Li, X. Wu, Y. Zhao, Z. Miao, L. Xing, J. Zhou, J. Zhao and S. Zhuo, *ChemElectroChem*, 2018, **5**, 1606–1614.
199 Y. Qiao, R. Zhang, R. Li, W. Fang, Z. Cui and D. Zhang, *Diamond Relat. Mater.*, 2021, **117**, 108488.
200 J.-S. Wei, S. Wan, P. Zhang, H. Ding, X.-B. Chen, H.-M. Xiong, S. Gao and X. Wei, *New J. Chem.*, 2018, **42**, 6763–6769.
201 X. G. Liu, Y. L. Wen, X. C. Chen, A. Dymerska, R. Wrobel, J. Y. Zhu, X. Wen, Z. F. Liu and E. Mijowska, *ACS Appl. Energy Mater.*, 2020, **3**, 8562–8572.
202 Q. Zhou, J. Chang, Y. Jiang, T. Wei, L. Sheng and Z. Fan, *Electrochim. Acta*, 2017, **251**, 91–98.
203 B. Chang, L. Wang, W. Shi, Y. Chai, S. Zhang and B. Yang, *Sustainable Energy Fuels*, 2020, **4**, 2527–2540.
204 C. Liu, F. Yi, D. Shu, W. Chen, X. Zhou, Z. Zhu, R. Zeng, A. Gao, C. He and X. Li, *Electrochim. Acta*, 2019, **319**, 410–422.
205 Z. J. Zhang, J. X. Li, T. T. Huang, M. R. Liu and X. Y. Chen, *J. Alloys Compd.*, 2018, **768**, 756–765.
206 G. X. Huang, Q. R. Liu, W. W. Kang, B. L. Xing, L. J. Chen and C. X. Zhang, *Electrochim. Acta*, 2016, **196**, 450–456.
207 H. Luo, Y. Yang, Y. Chen, J. Zhang and X. Zhao, *J. Appl. Electrochem.*, 2015, **46**, 113–121.
208 B. Xing, G. Huang, Z. Chen, L. Chen, G. Yi and C. Zhang, *J. Solid State Electrochem.*, 2016, **21**, 263–271.
209 G. Huang, W. Kang, Q. Geng, Q. Liu, B. Xing, C. Zhang, B. Duan and W. Wang, *J. Mater. Sci.: Mater. Electron.*, 2018, **29**, 10631–10639.
210 L. Xie, L. Kang, Y. Li, M. Cui, B. Chang, H. Jiang, L. Gao, X. Wang and S. Yun, *Nano*, 2017, **12**, 1750040.
211 G. Huang, Q. Geng, W. Kang, Y. Liu, B. Duan and C. Zhang, *J. Nanomater.*, 2018, **2018**, 1–9.
212 Z. J. Zhang, P. Cui, C. Chen, X. Y. Chen and J. W. Liu, *J. Solid State Electrochem.*, 2014, **18**, 59–67.
213 Z. J. Zhang, X. Y. Chen, D. H. Xie and P. Cui, *Electrochim. Acta*, 2014, **125**, 652–658.
214 D. Li, L. Chen, L. Chen, Q. Sun, M. Zhu, Y. Zhang, Y. Liu, Z. Liang, P. Si, J. Lou, J. Feng and L. Ci, *J. Power Sources*, 2019, **414**, 308–316.
215 S. H. Kang, B. N. Kim and I. G. Kim, *Energy Technol.*, 2019, **7**, 1801090.
216 W. Xiong, G. Yang, T. H. Yang, S. Liu and Y. Jung, *Bull. Korean Chem. Soc.*, 2017, **38**, 350–355.
217 X. Hu, Y. Wang, B. Ding and X. Wu, *J. Alloys Compd.*, 2019, **785**, 110–116.
218 K.-D. Seong, X. Jin, D. Kim, J. M. Kim, D. Ko, Y. Cho, M. Hwang, J.-H. Kim and Y. Piao, *J. Electroanal. Chem.*, 2020, **874**, 114464.
219 P. Zhang, M. Liu and S. Liu, *J. Mater. Sci.: Mater. Electron.*, 2020, **31**, 3519–3528.
220 L. Guan, L. Pan, T. Peng, T. Qian, Y. Huang, X. Li, C. Gao, Z. Li, H. Hu and M. Wu, *Carbon*, 2019, **152**, 537–544.
221 Y. H. Wang, B. Ding, D. Guo and X. L. Wu, *Microporous Mesoporous Mater.*, 2019, **282**, 114–120.
222 X. Luo, S. Li, H. Xu, X. Zou, Y. Wang, J. Cheng, X. Li, Z. Shen, Y. Wang and L. Cui, *J. Colloid Interface Sci.*, 2021, **582**, 940–949.

